Performance of HAGRID array in beta delayed neutron emission measurements

A Thesis Presented for the

Master of Science

Degree

The University of Tennessee, Knoxville

Thomas Tobias King

December 2018

© by Thomas Tobias King, 2018
All Rights Reserved.

For my family and friends, who have given me so much support an guidance during these last few years; and for my grandmother who taught me to never stop learning.

Abstract

One of the most prevalent decay modes of unstable nuclei is β[beta] decay. For nuclei far from stability these decays can be followed by the emission of a neutron. The Versatile Array of Neutron Detectors at Low Energy (VANDLE) is a proven detection system for measuring the energies of delayed neutrons. VANDLE has been upgraded to include high-efficiency scintillators for gamma-ray detection. This increases the sensitivity for the γ[gamma]-rays that can follow the neutron emission. These scintillator components form an array of large volume NaI detectors and the Hybrid Array of Gamma-Ray Detectors (HAGRiD), which is an array of $LaBr_3$[LaBr3] scintillators (BrilLanCe 380™). An experimental campaign at the Holifield Radioactive Ion Beam Facility at Oak Ridge National Laboratory was completed in the Spring of 2016. Beams of several ^{238}U[238U] fission fragments were delivered to VANDLE. Some of the advantages and drawbacks of the new γ[gamma]-ray systems, in particular HAGRiD, will be presented in this work through the results for the decays of two neutron rich Rubidium isotopes (^{94}Rb [94Rb] and ^{97}Rb [97Rb]).

Table of Contents

1 Motivation **1**

1.1 Introduction . . . 1

1.2 Beta-delayed Neutron Emission . . . 3

1.2.1 Beta Decay . . . 3

1.2.2 Allowed Beta Decay Transitions . . . 5

1.2.3 Beta-delayed Neutron Decay . . . 6

2 Hybrid Arrays for Beta Delayed Neutron Studies **8**

2.1 Motivation for Hybrid Neutron-Gamma Arrays . . . 8

2.2 Examples of Hybrid Arrays for βn Studies . . . 9

2.2.1 Neutron Energy Arrays . . . 9

2.2.2 Neutron Counters . . . 10

3 VANDLE As A Hybrid Array **14**

3.1 VANDLE . . . 14

3.2 Neutron Detection . . . 14

3.2.1 Beta Detectors . . . 15

3.2.2 Specifics of VANDLE . . . 16

3.3 Gamma-ray Detection . . . 18

3.3.1 High Purity Germanium Detectors . . . 18

3.3.2 Sodium Iodide . . . 19

3.3.3 Lanthanum Bromide . . . 20

3.4 Digital Data Acquisition System . . . 22

3.5 Tape Transport System . . . 23
3.6 PAASS . . . 25

4 VANDLE's Evolution **27**
4.1 Initial development . . . 27
4.2 ORNL 2012 LERIBSS Campaign . . . 27
4.3 VANDLE Implementation at CARIBU (Argonne National Lab) . . . 28
4.4 CERN ISOLDE Decay Station . . . 29
4.5 ORNL 2016 OLTF . . . 30
4.6 2016 NSCL experiment (E14060) . . . 32
4.7 VANDLE at RIBF (RIKEN) . . . 33

5 Beta-delayed neutron spectroscopy of fission fragments at ORNL **36**
5.1 Physics Justification . . . 36
5.2 Description of the Facility and Beam Production . . . 39

6 Analysis Methods **41**
6.1 Basic Analysis Methods of HAGRiD and VANDLE data . . . 41
6.1.1 Full Energy Reconstruction with HAGRiD and NaI . . . 41
6.1.2 Analysis of Hybrid Data . . . 42
6.2 Challenges . . . 42
6.2.1 ^{138}La Contamination . . . 42
6.2.2 New Beta Detector . . . 43
6.2.3 Large Data Volume . . . 43
6.3 Detector Calibrations . . . 46
6.3.1 HPGe Calibrations . . . 46
6.3.2 Scintillators . . . 47
6.4 Gamma-Ray Efficiency . . . 49
6.5 Analysis of hybrid data from HAGRID and VANDLE . . . 50
6.5.1 Full Energy Reconstruction . . . 52
6.5.2 Neutron Calibration and n-γ Analysis . . . 53

7 Results of Full Energy Reconstruction and Hybrid Analysis **56**

7.1 ^{94}Rb 57

7.1.1 Full Energy Reconstruction 57

7.1.2 Neutron-γ Coincidence 61

7.2 ^{97}Rb 65

7.2.1 Neutron-γ Coincidence 65

8 Summary **69**

Bibliography **71**

Vita **77**

List of Figures

1.1 Fission Yields for ^{235}U. The blue boxes indicate the regions of the chart that are part of the experiment which is the subject of this work [2] 2

1.2 Plot of the nuclear deformation. The color indicates what type of deformation based on the UNEDF0 model [3]. The pink dots and squares are indicators of the probablility of neturon emission [4]. 2

1.3 Chart of the Nuclei [2]. The pink and blue regions represent the areas where β^- and β^+ decays are prevalent. The yellow squares show alpha emitting nuclei, and nuclei represented by the green squares are dominated by fission. 3

1.4 Schematic illustration relating S_β, and the intensity observed (I_β) 4

1.5 Chart of the Nuclides showing the energy window available for beta delayed neutron emission using Q_β- $S_n$from recent mass evaluation. [9] [10] 7

1.6 Schematic illustration of β-delayed neutron decay process 7

2.1 TONNERRE in its hybrid setup [11] 10

2.2 MTAS without its external shielding. 11

2.3 ^{89}Br decay in MTAS. The black line is the total MTAS spectrum, the yellow line is the gate on high energy in the outer modules indicating the detection of a neutron, and the blue is the coincident central module spectrum.[13] . . 12

2.4 Hybrid-3Hen as implemented at HRIBF's LERIBSS. [14] 13

2.5 BRIKEN in hybrid-mode (left, and front) at F11 in RIBF at RIKEN [16] . . 13

3.1 VANDLE Modules 17

3.2 Cartoon depiction of a Time of Flight measurement. [17] 18

3.3 HPGe Clover detector used by VANDLE. Seen here with the pre-amp casing open. 19
3.4 NaI detector used with VANDLE at the ORNL2016 and NSCL2016 experiments 20
3.5 Experiment room background most of the counts are from the ^{138}La or ^{227}Ac. These data was taken over the course of about two days. The total of the sixteen HAGRiD detectors are shown in blue while the total of the four HPGe from the clover is in red 21
3.6 Spectra taken with ^{137}Cs and ^{60}Co sources. Again HAGRiD is shown in blue while the HPGe is in red 22
3.7 2" HAGRiD ($LaBr_3$:Ce) used with VANDLE at the ORNL2016 and NSCL2016 experiments 22
3.8 Left: Pixie16 Rev F card. Right: Pixie Crate containing 8 Pixie16 Cards for 128 channels 23
3.9 Picture of the inside of the shielded MTC drive. The tape enters near the arrow on the top left. The extra tape is stored in the square internal box, before going through the tensioning mechanism and then back to the implantation point through the same beam pipe it entered from. 25

4.1 Original VANDLE setup at LERIBSS. Not pictured are the HPGe clovers but the mounts are visible to the left and right of the beampipe in the middle of the arcs 28
4.2 Left: New β detection system utilizing SiPMs. Right: Argonne National Laboratory configuration 29
4.3 ISOLDE IDS setup from 2017. 30
4.4 Left: Full Arc of Medium Bars as implemented at the OLTF in February of 2016. Right: Drawing of the new gamma-ray system. In yellow is the HPGe Clover, red is the NaI array, and blue are the 2" HAGRiD detectors. The beampipe is semi-transparent for clarity 31

4.5 The γ-ray system as implemented at the NSCL in October 2016. The arrow indicates the beam direction. In the cut away of the beam pipe sits the PSPMT implantation detector. Here the HAGRiD are in blue, NaI in red, and the Clover is brown. 32
4.6 Left: Old medium bar support system. Right: New medium bar support system. 33
4.7 Isometric view of the new frame for RIKEN. Arrow represents the beam direction. 35

5.1 Nilsson Diagram for 50 < N < 82. Marked are the active neutron orbitals near the Fermi energy for N=56. 38
5.2 The On-Line Test Facility (OLTF) of the Holifield Radioactive Ion Beam Facility at Oak Ridge Nation Laboratory. 40

6.1 Beta System for the 2016 ORNL experiment. 44
6.2 Efficiency of the β detector as a function of subsequent γ-ray energy as seen in the clover. 45
6.3 Comparison of 1577 keV γ-ray from ^{94}Rb calibrated with 1 or 2 functions. Red is with two functions, blue is with a single function. 47
6.4 Comparison of ^{94}Rb data calibrated by sources and with internal calibrations. The red and burgundy lines are the HPGe data. The blue lines are the HAGRiD data; light blue is the in-data calibration and dark blue is using only source data for calibration 48
6.5 CAD render of the γ-ray detector stack with group labels. 49
6.6 Efficiency curves for the three different subsystems of the γ-ray array 50
6.6 Efficiency curves for the various types of γ-ray detector systems 52
6.7 Top: Bar vs Time of Flight after alignment. Below: Bar vs Time of Flight before alignment 54
6.8 Upper: Clover energy vs β-γ time difference. Lower: HAGRiD energy vs β-γ time difference 55

7.1 Clover singles vs β-gated singles in ^{94}Rb 57

7.2 Spectrum of clover energy vs total energy deposited into the gamma-ray system for ^{94}Rb 58
7.3 Level Diagram for ^{94}Rb. Showing only the lower 3 MeV of the nucleus. Marked are the six γ-rays shown in Figure 7.4. [34][2] 59
7.4 Results for ^{94}Sr level reconstruction 60
7.5 Coincident γ-ray decay scheme for ^{97}Rb βn decay [34] 61
7.6 Comparison of neutron time-of-flight vs VANDLE QDC for the clover (top) and the HAGRiD (bottom) when gated on the 432.5 keV γ-ray 62
7.7 Comparison of VANDLE ToF spectrum to existing ^{94}Rb data 63
7.8 Preliminary Neutron-γ results for ^{94}Rb 64
7.9 Coincident γ-ray decay scheme for ^{97}Rb βn decay [36] 65
7.10 Preliminary ToF spectrum in VANDLE when gated on the 815 keV γ-ray . 66
7.11 Comparison of VANDLE ToF spectrum to existing data for ^{97}Rb 67
7.12 Comparison of neutron time-of-flight vs VANDLE QDC for the high statistics (upper) and low statistics (lower) data sets 68

Chapter 1

Motivation

1.1 Introduction

The subject of this work is to demonstrate the performance of the Hybrid Array of Gamma-Ray Detectors (HAGRiD) which complements the Versatile Array of Neutron Detectors at Low Energy (VANDLE) in the measurements of the decays of ^{238}Uranium fission fragments. These nuclei are of interest for multiple fundamental research and application topics. As seen in Figure 1.1, the four elements measured in this experiment (Rubidium, Cesium, Bromine, and Iodine) are produced in abundant quantities in the fission of ^{238}U. Of particular interest to nuclear structure are the rubidium isotopes, because as seen in Figure 1.2 they range from spherical to deformed. The lighter rubidium isotopes measured during this experiment ($^{93\text{-}96}$Rb) are spherical while the heaver nuclei ($^{97\text{-}100}$Rb) are highly deformed. Theoretical studies by Krumlinde *et al.*[1] show that the deformation has an effect on the beta-decay strength function in Rubidium isotopes. The decays of the nuclei in the four measured isotopic chains are also important for the modeling of reactor decay heat. This decay heat is an important parameter in nuclear reactor design and function; necessitating reliable input data. These nuclei have been studied in the past with other experimental techniques. This work will focus on the beta-delayed neutron spectroscopy of ^{94,97}Rb with the hybrid VANDLE-HAGRiD array.

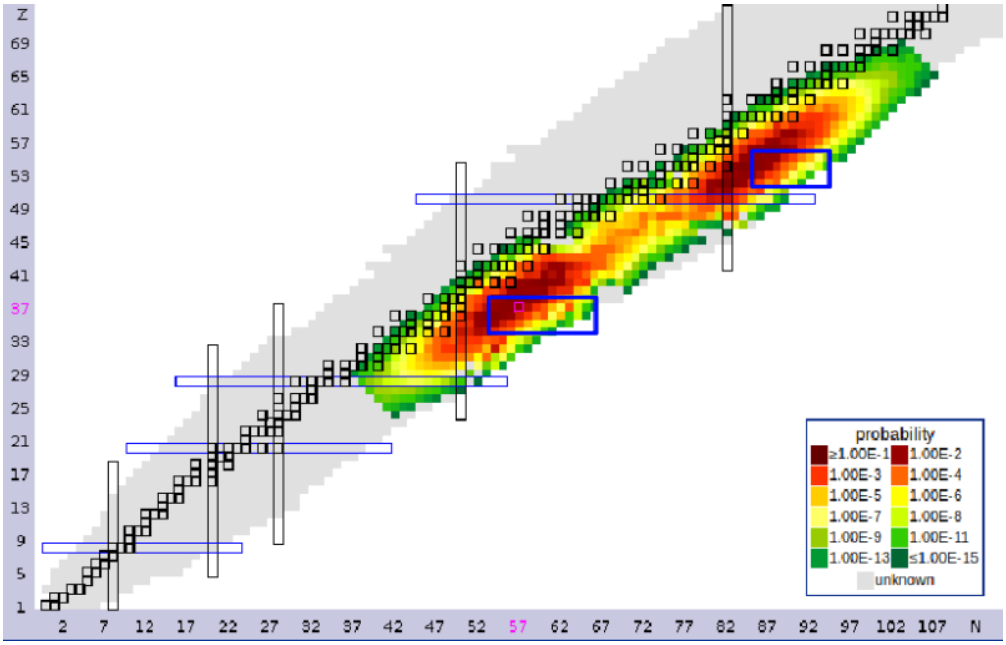


Figure 1.1: Fission Yields for ^{235}U. The blue boxes indicate the regions of the chart that are part of the experiment which is the subject of this work [2]

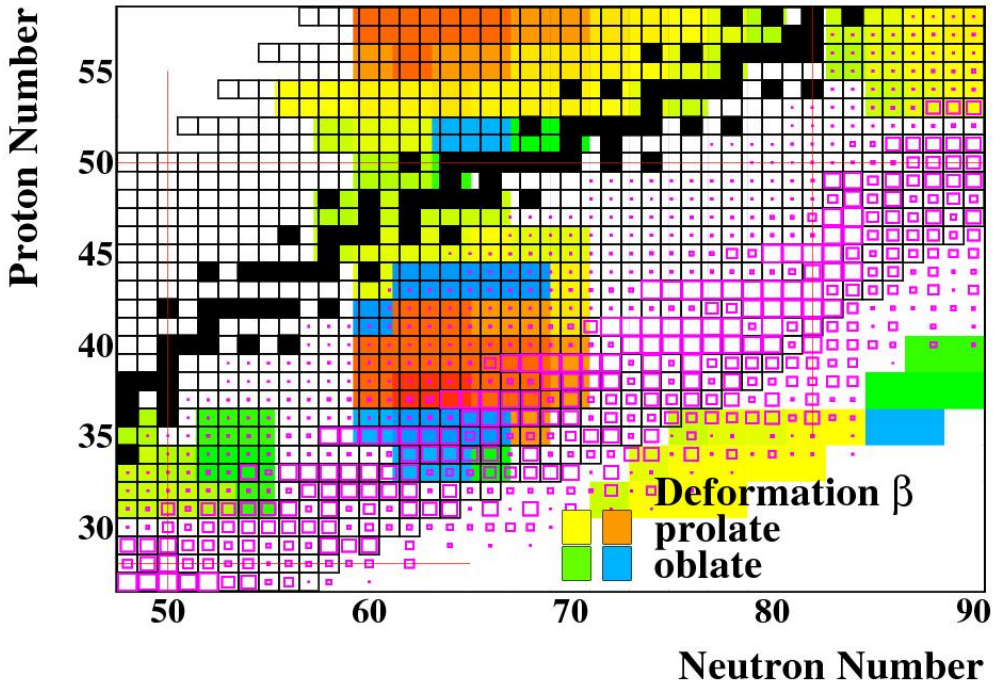


Figure 1.2: Plot of the nuclear deformation. The color indicates what type of deformation based on the UNEDF0 model [3]. The pink dots and squares are indicators of the probablility of neturon emission [4].

1.2 Beta-delayed Neutron Emission

1.2.1 Beta Decay

As seen in Figure 1.3; one of the major decay modes for unstable nuclei is beta decay. This process leave the mass number of the nucleus unchanged but converts individual neucleons. As seen in Figure 1.3, for neutron-rich nuclei the β^- decay is a process by which a neutron is converted into a proton, with an electron and an anti-neutrino being emitted. For proton-rich nuclei, β^+ decay is a converting a proton into a neutron,with the emission of a positron and a neutrino. The process of β^- decay can be written schematically as ${}^A_Z X_N \Rightarrow {}^A_{Z+1} X_{N-1} + e^- + \bar{\nu}_e$ or ${}^A_Z X_N \Rightarrow {}^A_{Z-1} X_{N+1} + e^+ + \nu_e$ for β^+ [5]. Additionally, electron capture is a type of β decay which may occur in parallel to β^+. In that process an inner shell atomic electron is captured by the nucleus; turning a proton into a neutron and emitting an election neutrino.

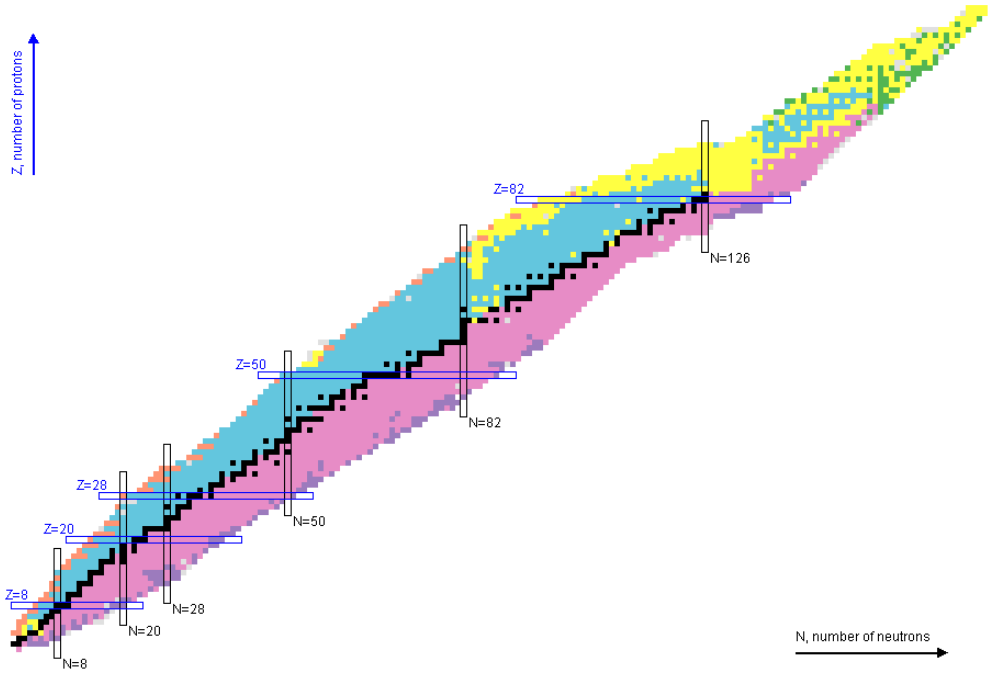


Figure 1.3: Chart of the Nuclei [2]. The pink and blue regions represent the areas where β^- and β^+ decays are prevalent. The yellow squares show alpha emitting nuclei, and nuclei represented by the green squares are dominated by fission.

These decays can, and often do, leave the decay daughters in an excited state. For nuclei close to stability, the daughter de-excites via gamma emission. The beta decay half life is

given by Equation:1.1. Where $Q_\beta$represents the energy window for the beta decay, and E_i represents the final level's energy.

$$t_{\frac{1}{2}}^{-1} \sim \sum_{E_i \geq 0}^{E_i \leq Q_\beta} S_\beta(Q_\beta) \cdot f(Z, Q_\beta - E_i) \tag{1.1}$$

In Figure 1.4 and Equation 1.1, S_β is the beta decay strength function; this is an expression of the transition matrix probabilities and the beta-decay transition operator. The second term in Equation 1.1 represents the role of phase space in the process which involves the emission of two leptons and the sharing of the decay energy. The Fermi integral has a f $\sim E^5$ behavior, this means that as the transition energy goes up (i.e. decays to lower excited states in the daughter nucleus) the value of Fermi integral increases significantly. This tends to suppress the observed intensity of decays (I_β) to the higher excitation energy states, and enhance the decays to the lower energy states. This can be see graphically in figure 1.4. For decays that populate states above the neutron separation energy, S_n a neutron can emitted; subsequently, states above the two-neutron separation energy, S_{2n} can emit 2 neutrons.

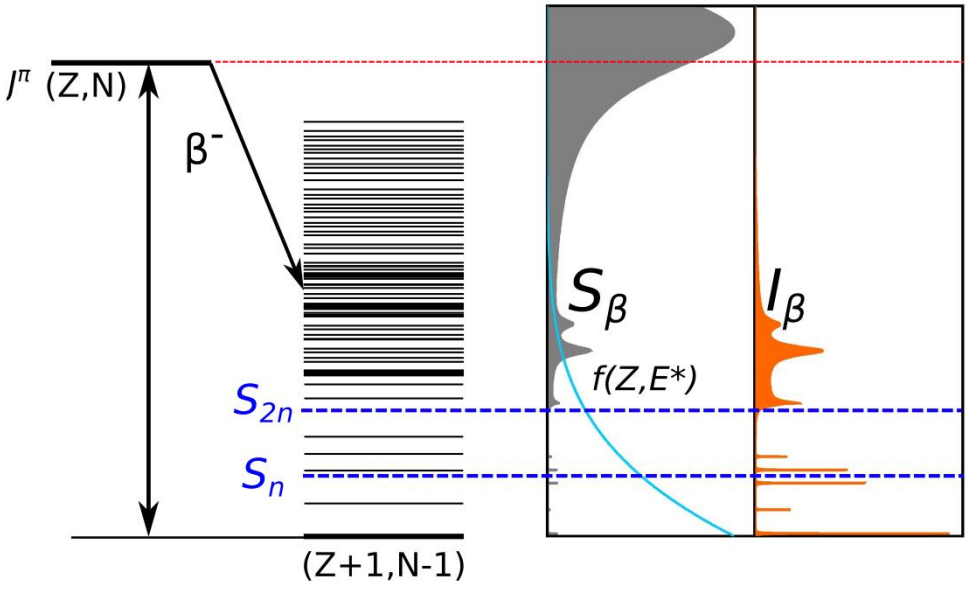


Figure 1.4: Schematic illustration relating S_β, and the intensity observed (I_β)

Beta decay can be categorized into allowed transitions and forbidden transitions. Allowed transitions are those with no change in the orbital angular momentum of the nucleus, while

in forbidden transitions the emitted particles (e^- and $\bar{\nu_e}$ for β^-; e^+ and ν_e for β^+) remove some amount of orbital angular momentum from the nucleus [5]. First forbidden (FF) transitions, which are the most common type of forbidden transitions, are generally less probable than allowed transitions [6], although the effects of phase space and fragmentation of allowed decay strength in the decay can mask this. First Forbidden transitions always have a change of the orbital angular momentum of ± 1 and a change in parity. A parameter often used to describe β decay is the comparative half-life, $ft_{1/2}$. This value represents the Fermi integral evaluated for the specific transition between the mother's initial state and daughter's final state; multiplied by the β decay half-life. Because of the broad range of the transition matrix elements, ft spans a large range of values; so it is generally described as the $\log_{10} ft$. A log ft between 3 and 6 is indicates an allowed transition, while a value of greater than 6 is generally forbidden.

1.2.2 Allowed Beta Decay Transitions

The allowed categories of beta decay can be further broken into Fermi (Equation:1.2) and Gamow-Teller (Equation:1.3) decays. Both of these operators are written with the isospin ladder operator, $\tau^{\pm}$. In Fermi transitions, the emitted leptons have spins that are anti-parallel. This allows for transitions with no net change in angular momentum.

$$\sum_{i=1}^{A} \tau^-(i) \qquad \text{Fermi type} \tag{1.2}$$

$$\sum_{i=1}^{A} \vec{\sigma}(i)\tau^-(i) \qquad \text{Gamow-Teller type} \tag{1.3}$$

Gamow-Teller type transitions are the most abundant type of decays [7].The Pauli spin operator, $\vec{\sigma}(i)$, allows for decays between spin-orbit partners in the single particle picture. Gamow-Teller transitions are defined by allowing a change of ± 1 or 0 in the isospin and the total angular momentum, while keeping the parity and orbital angular momentum the same.

1.2.3 Beta-delayed Neutron Decay

For nuclei where the beta decay energy (Q_β) exceeds the neutron separation energy (S_n) particle emission becomes energetically possible . This two-step process is beta-delayed neutron emission. It becomes increasingly more probable as the nuclei get farther away from stability, the Q_β increases and the S_n decreases (see Figure 1.5). In nuclei with a large asymmetry between the number of proton and neutrons, the valence neutrons do not have spin-orbit partners that are near the Fermi energy. The neutron that decays is from a spin-orbit partner of the valence proton shell, leaving a hole deep in the core, leaving the nucleus in a highly excited state [8]. For nuclei close to stability, the nucleus de-excites via the emission of γ-rays, as the nucleus equilibrates. But for nuclei farther from stability, it is possible that the excess energy is enough to emit one (or more) of the valence neutrons. This is a multi step process; the initial beta decay and the subsequent de-excitation of the daughter. The full beta-delayed neutron emission can be schematically written as:

$$ {}^{A}_{Z}X_N \Rightarrow {}^{A}_{Z+1}Y_{N-1} + e^- + \bar{\nu}_e \Rightarrow {}^{A}_{Z+1}Y_{N-2} + n \tag{1.4} $$

and is drawn in Figure:1.6. However, since the neutron emission does not generally leave the granddaughter in the ground state the daughter must de-excite. This occurs via the emission of γ-rays. Thus to gather a complete picture of the nucleus both γ-rays and neutrons must be measured in coincidence with a combination detector system.

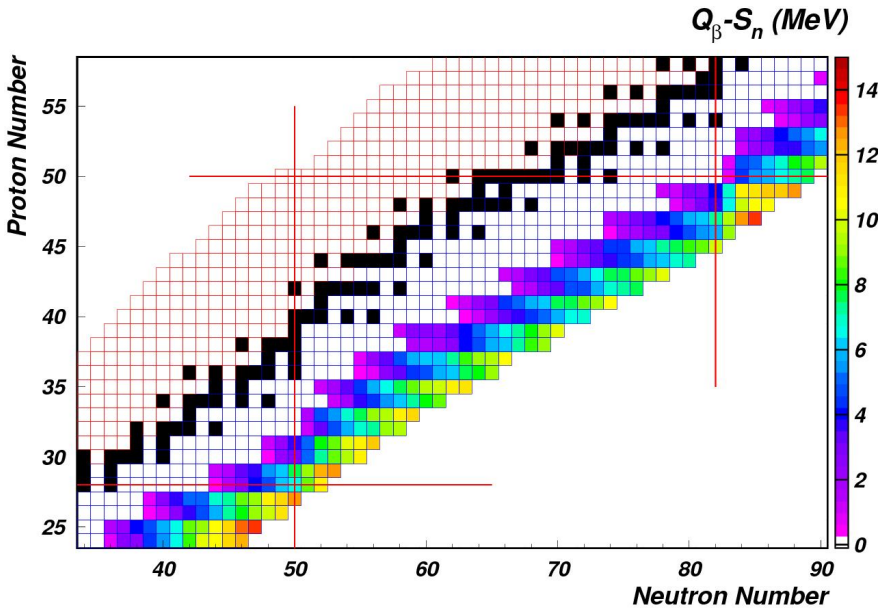


Figure 1.5: Chart of the Nuclides showing the energy window available for beta delayed neutron emission using Q_β- $S_n$from recent mass evaluation. [9] [10]

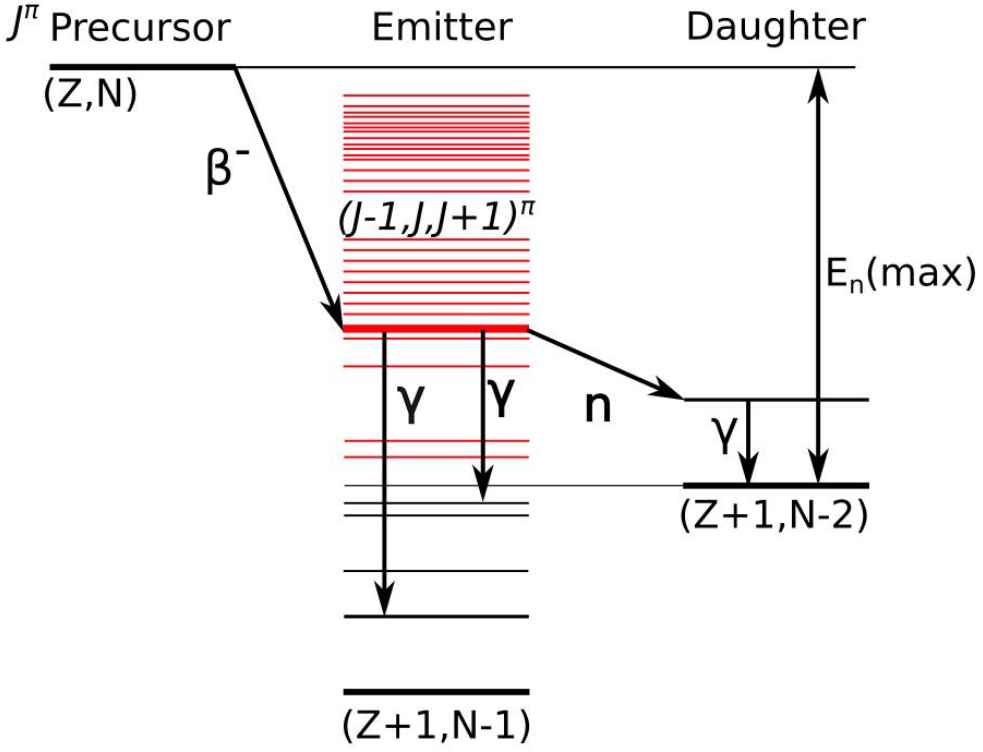


Figure 1.6: Schematic illustration of β-delayed neutron decay process

Chapter 2

Hybrid Arrays for Beta Delayed Neutron Studies

2.1 Motivation for Hybrid Neutron-Gamma Arrays

Beta-delayed neutrons are frequently followed by the emission of gamma-rays. This necessitates measuring these gamma-rays in coincidence with the neutrons, to properly reconstruct the level scheme. Hybrid arrays typically sacrifice the detection efficiency of a single radiation type to gain efficiency to multiple types. For beta delayed neutron arrays some of the neutron efficiency is given up for the addition of γ-ray detectors. This is because of the division of the solid angle between neutron and γ-ray detection. The goal of hybrid arrays is to maximize the detection efficiency for all desired radiation types. One of the more straight forward methods to measure the neutron's energy is with Time of Flight (which will be discussed in detail in the next chapter) Put simply it uses the time difference between the beta decay at the implantation site and the neutron detection at a known distance from the implantation site,to determine the energy. For these arrays, a longer flight path leads to better energy resolution however this requires either larger detectors or many more of them to maintain the solid angle efficiency.

2.2 Examples of Hybrid Arrays for βn Studies

Briefly described here are different neutron arrays for βn studies. These arrays were used for neutron spectroscopy (2.2.1) or for counting neutrons to find P_n (2.2.2).

2.2.1 Neutron Energy Arrays

These arrays are designed to be as efficient as possible, while maintaining the required neutron energy resolution. By combining the energy of the detected neutron with that of the subsequent γ-ray(s), a full picture of the decay scheme can be deduced. This informs the general structure of the emitter nucleus.

TONNERRE

One of the hybrid-Time of Flight arrays used for spectroscopy of exotic nuclei was TONNERRE (seen in Figure 2.1). In this configuration a maximum of 15 TONNERRE modules was used, along with 6 of the smaller LEND (another neutron detector array) modules and 2 HPGe detectors from the MINIBALL array [11]. TONNERRE used curved plastic scintillators (160 x 20 x 4 cm^3 volume) for neutron detection with a 120 cm flight path. LEND uses the same plastic scintillator as TONNARRE but had a smaller volume, with a 66 cm flight path. The TONNERRE+LEND array had an efficiency of ∼7.7% and ∼2% respectively. It was used at CERN ISOLDE for measurements of the decays of $^{51\text{-}53}$K [11].

Modular Total Absorption Spectrometer

While not a true hybrid array, the Modular Total Absorption Spectrometer (MTAS) is sensitive to neutrons as well as γ-rays [12]. The MTAS is an array of 19 NaI(Tl) detectors, weighing approximately 1000 kg. Seen in Figure 2.2 is MTAS without its sheilding. MTAS is designed to detect large γ-ray cascades to reconstruct the initial decaying level. However because of the high mass and large cross-section of neutron capture on iodide, it has the ability to detect neutrons as well [12]. MTAS has enough mass to thermalize the neutrons through inelastic scattering, ^{137}I(n,n'γ), interactions. Once the neutrons have

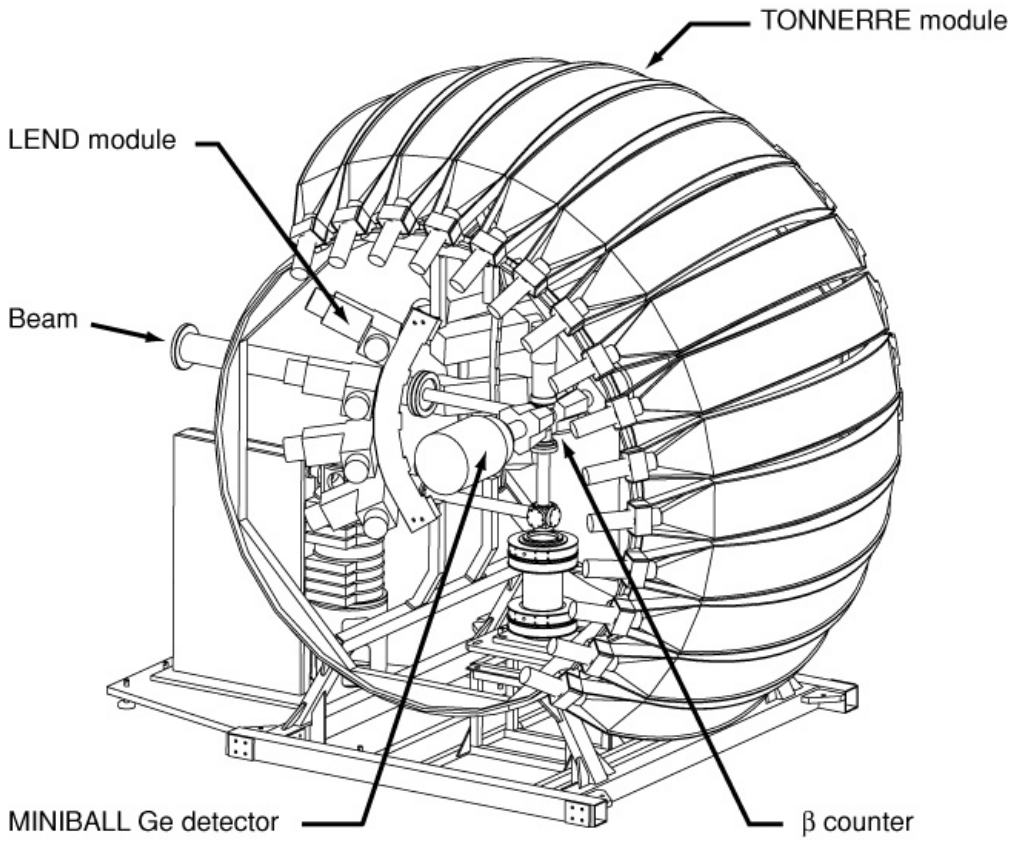


Figure 2.1: TONNERRE in its hybrid setup [11]

been thermalized, they are captured by the Iodine which gives about 6 MeV of energy. If the capture peak is detected, it is summed with the preceding 58 keV ^{137}I(n,n'γ) γ-rays, which were detected away from the middle of the spectrometer. However, the resolution for neutrons is limited by the intrinsic resolution for the final capture, which is approximatly 250 keV for background thermal neutrons, and is expected to be similar for β-delayed neutrons [12]. Shown in Figure 2.3 is an MTAS spectra for the decay of ^{89}Br. By gating on the capture peak in the outer modules and looking at what the central module, it can be seen that they are able to see the known γ-rays following beta-delayed neutron emission [13].

2.2.2 Neutron Counters

These detector arrays are designed to maximize the neutron detection efficiency. This allows these arrays to measure the branching ratios (P_n, P_{2n}, etc.) at the very low beam rates for nuclei far from stability .

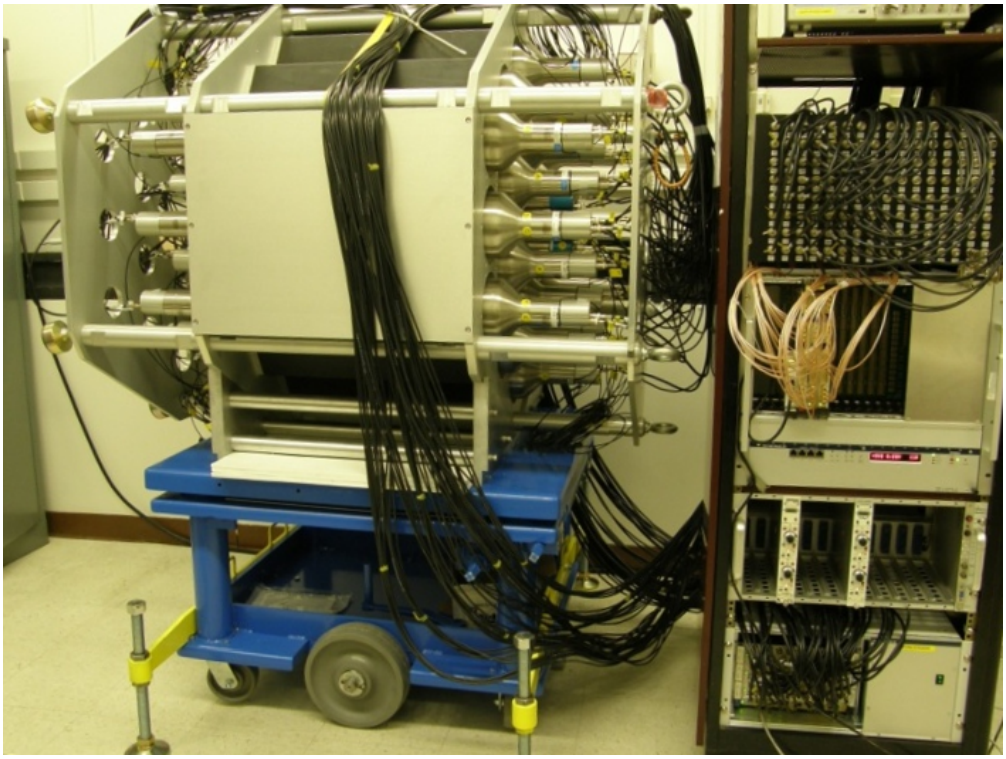


Figure 2.2: MTAS without its external shielding.

Hybrid-3Hen

One such hybrid array is Hybrid-3Hen [14]; this array consists of two HPGe clover type detectors and 48 2" ^{3}He tubes. The ^{3}He tubes are placed in a high-density polyethylene (HDPE) moderator. This array uses the same electronics and Moving Tape Collector system as VANDLE (Chapter 3) and other HRIBF detector arrays; it also borrows the Clover detectors from CLARION/CARDS arrays. The HDPE moderates the emitted neutrons down to thermal energies where the neutron capture cross-section on ^{3}He is the highest. The Hybrid-3Hen implementation resulted in an average neutron detection efficency of ∼30% [14].

BRIKEN

The successor to Hybrid-3Hen is BRIKEN (seen in Figure 2.5). It combines ^{3}He tubes from 3Hen with other ^{3}He detectors to create the largest β-delayed neutron counter for nuclear physics in the world [15]. BRIKEN, in hybrid mode, consists of 140 ^{3}He proportional counters

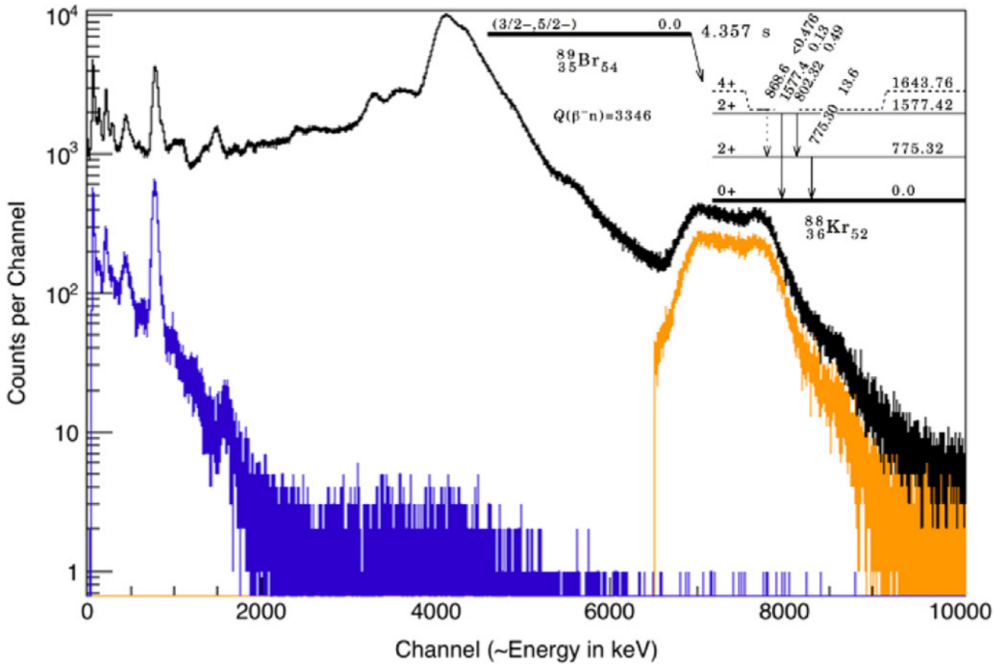


Figure 2.3: ^{89}Br decay in MTAS. The black line is the total MTAS spectrum, the yellow line is the gate on high energy in the outer modules indicating the detection of a neutron, and the blue is the coincident central module spectrum.[13]

with 2 clover type HPGe detectors [16]. These HPGe detectors are of the same type as those used by Hybrid-3Hen and by VANDLE. The additional ^{3}He tubes increases BRIKEN's nominal neutron detection efficiency to approximately 66% [16].

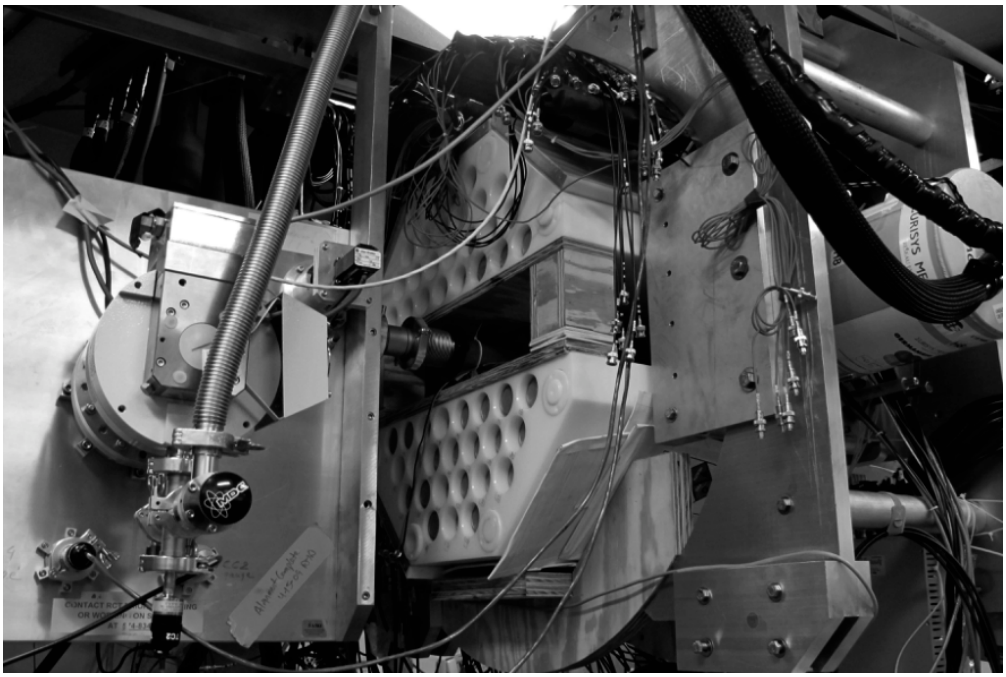


Figure 2.4: Hybrid-3Hen as implemented at HRIBF's LERIBSS. [14]

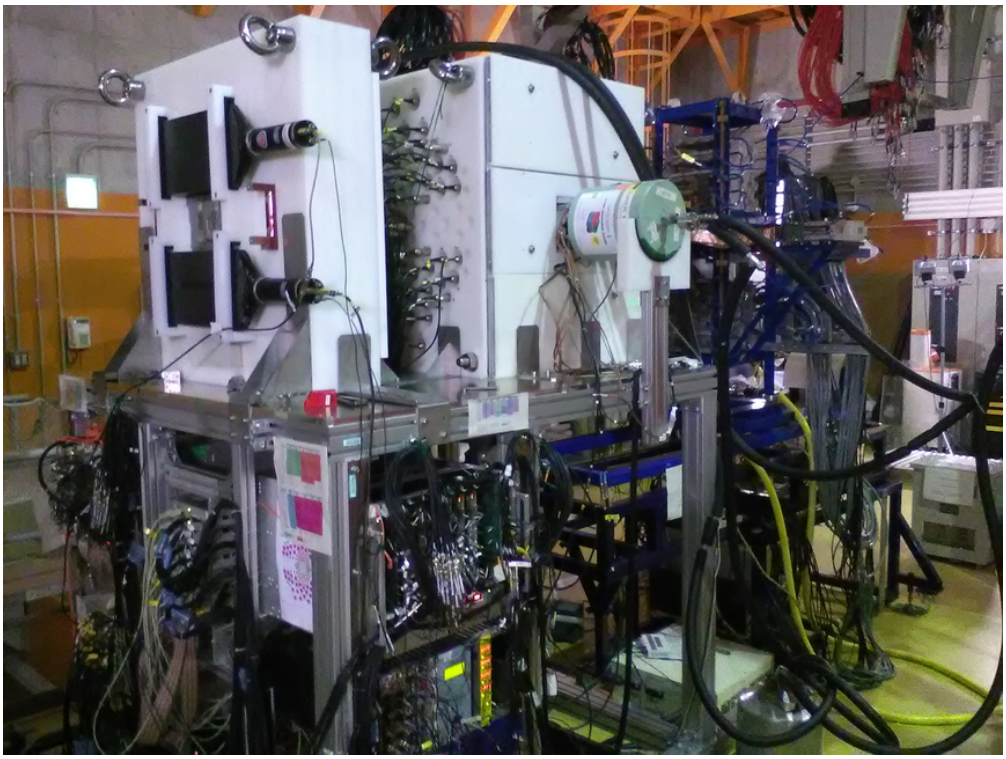


Figure 2.5: BRIKEN in hybrid-mode (left, and front) at F11 in RIBF at RIKEN [16]

Chapter 3

VANDLE As A Hybrid Array

3.1 VANDLE

The Versatile Array of Neutron Detectors at Low Energy (VANDLE) is a Time of Flight (ToF) array using plastic scintillator bars. VANDLE is similar to TONNERRE (2.2.1) but aims to be more flexible and capitalize on newer materials and electronics. VANDLE's implementation of the Time of Flight method for determining the emitted neutron energy will be discussed in more detail in a later section (3.2) of this chapter. The ToF method relies on precise measurements of the time for the β decay and the neutron's interaction with VANDLE for determining the energy of the emitted neutron. The digital data acquisition system (DAQ) achieves fast timing and has the flexibility to couple VANDLE with other ancillary systems, whether that is other detector systems, such as germanium detectors or logic signals, like those coming from the Moving Tape Collector's controller.

3.2 Neutron Detection

As mentioned earlier (3.1), VANDLE uses the Time of Flight (ToF) method for determining the emitted neutron energy.This method uses the initial β decay as the start event, and the neutron's detection in the bar as a stop. The time difference of these two signals along with the known flight path, give the velocity of the neutron. The energies of β-delayed neutrons, typically a few MeV or less, are non-relativistic such that $E = \frac{1}{2}mv^2$ is still valid. The

neutrons, being uncharged, are hard to detect directly. In plastic scintillators, when the neutron enters the material it can inelastically scatter off the hydrogen atoms causing them to recoil. The recoiling proton produces the light that is detected by the PMTs. The plastic is doped with a wavelength shifter, which shifts the light into the wavelength where the conversion efficiency of the PMT is highest. This shift generally puts the photons in the blue region of the visible spectrum. The neutrons can also scatter off of the other elements in the plastic, mainly carbon and oxygen, but due to the differences in mass these recoils are much smaller and therefore produce much less light. The scintillation light travels down the bar, where it interacts with the photocathode of the PMTs; producing electrons. These electrons are accelerated and amplified by the PMT, and the signal that is read-out is large enough to be digitized but is still directly proportional to the amount of light that originally interacted with the photocathode. However, because the amount of light produced depends on the neutron scattering kinematics and because not all of the neutron's energy is deposited in the detector, the amount of light is not directly related to the energy of the neutron.

3.2.1 Beta Detectors

Since VANDLE uses the initial β decay as the start of the timer for the time of flight of the neutron. It is necessary to have a detector for the β particles. In general VANDLE has three requirements from the β detector; first and most important is good timing resolution. Since VANDLE relies on the time difference between the β decay and the arrival time of the neutron at the bars, having a β detector with poor time resolution degrades the separation between neutrons of different energies. Additionally, a high efficiency β detector is also needed. A low efficiency β detector means an increased signal to background ratio in the VANDLE bars themselves, through an increase in uncorrelated events. The third thing is for the β detector to be as compact as possible while not compromising the other criteria. By making the detector compact, we decrease the amount of material around the decay point, leading to less absorption of the γ-rays, as well as less scattering of neutrons. Specifics of the individual detector systems used with VANDLE will be discussed in the next chapter, as this is an area that has had significant evolution since the first VANDLE experiment.

3.2.2 Specifics of VANDLE

The VANDLE array has 3 sizes of bars; small, medium and large (seen in Figures 3.1a and 3.1b). The small bars have a 3 cm x 3 cm cross section and are 60 cm long; with a 1 inch photomultiplier tube (Hamamatsu R580) on each end. The medium bars are 6 cm wide by 3 cm thick and are 120 cm long with a small taper on the ends which brings the width down to ∼5 cm. The large bars have a 5 cm by 5 cm profile and are 200 cm long. Both the medium and large bars are coupled with 2 inch PMTs (Hamamatsu R7724). All of the bars have an outer wrapping of single sided aluminized mylar. The small bars have a inner wrapping of nitrocellulose paper, while the medium and large bars have thin double-sided aluminized mylar.

Generally the small bars are configured with a flight path of 50 cm, and the medium bars with a path of 100 cm. VANDLE's energy resolution is given by Equation 3.1, where T is the time, E is the energy of the neutron and r is the path length.

$$\left(\frac{E}{dE}\right)^2 = \left(\frac{2dT^2}{T}\right) + \left(\frac{2dr^2}{r}\right) \tag{3.1}$$

Since our timing resolution is finite and dr which is the uncertainty in the path length is fixed by the physical thickness of the bar, one easy way to increase the energy resolution is to increase the flight path. This was the motivation for the medium sized bar; which were designed to have the same solid angle coverage at 1 m as the small bars at 50 cm while maintaining the same dr. However this has diminishing returns since longer flight paths may introduce a detection threshold. The detection threshold comes from decreasing photon collection efficiency because of multiple scattering in the long detector. Setting the electronic threshold too low increases the uncorrelated background rate, which causes an increase in the background. So a balance must be achieved, where we minimize $\frac{dr}{r}$ while also minimizing the uncorrelated rate. The balance can change depending on the specifics of the experiment being preformed, for example if a large amount of high energy neutrons is expected then the flight path could be increased, assuming that the random rate is low, at the expense of some solid angle efficiency, and vise versa if we expect more medium to low energy neutrons the flight path could be decreased to increase the solid angle coverage at the expense of the



(a) Medium bars during the gluing stage of assembly.



(b) Large, Medium and Small module for size comparison

Figure 3.1: VANDLE Modules

resolution for higher-energy neutrons. The fact that VANDLE's modules are straight allows for this increased flexibility in the experimental setup over the older TONNERRE modules, which were curved for a specific radius. However, being straight means that a correction is required to correct the flight length near the ends of the bars, as seen in Figure 3.2; while not hard to implement it does impact the measurements.

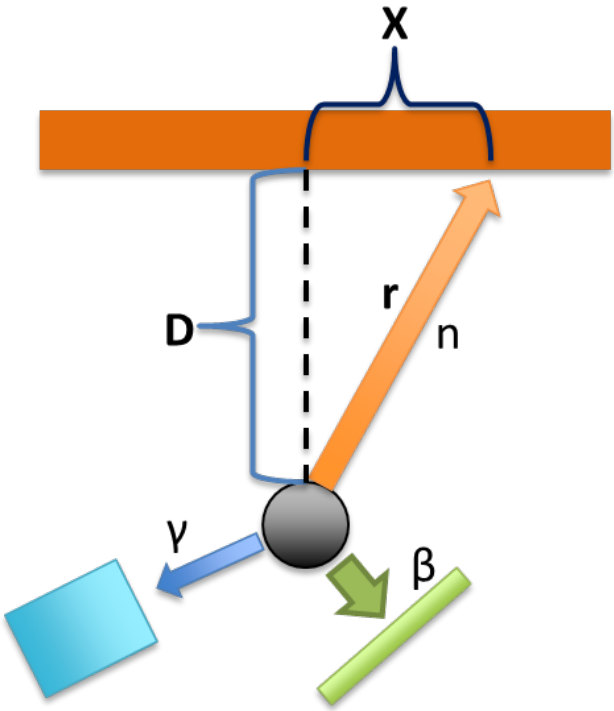


Figure 3.2: Cartoon depiction of a Time of Flight measurement. [17]

3.3 Gamma-ray Detection

The VANDLE system can be coupled with a variety of gamma-ray detectors. The number of gamma-ray detectors, along with which types and their arrangement, has evolved with VANDLE. This evolution will be discussed in the next chapter.

3.3.1 High Purity Germanium Detectors

High-Purity Germanium Detectors (HPGe), in particular HPGe clovers, were the first γ-ray detectors coupled with VANDLE (seen in Figure 3.3). The clovers consist of four HPGe

crystals in a 4 leaf clover style arrangement, when viewed from the detector face. One of the benefits of HPGe detectors is their high γ-ray resolution. This allows for the separation of close lying γ transitions, and helps with the identification of beam contaminates. But their benefits come at a cost, HPGe detectors generally have poor efficiency due to their smaller size; and require the use of liquid nitrogen (LN_2).

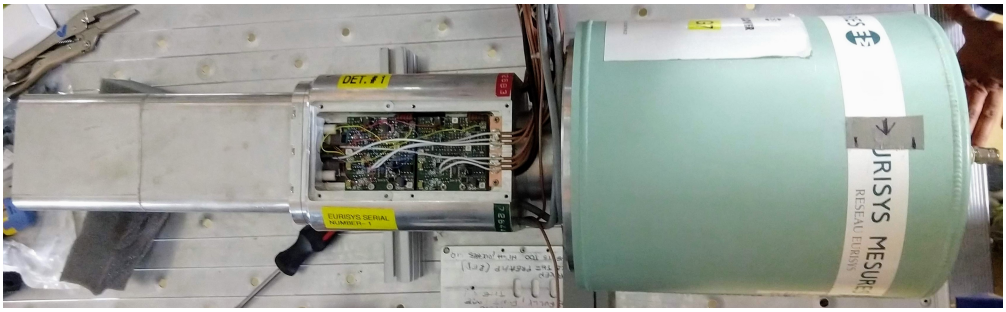


Figure 3.3: HPGe Clover detector used by VANDLE. Seen here with the pre-amp casing open.

3.3.2 Sodium Iodide

A need for more γ-ray efficiency was identified and lead to the addition of sodium-iodide (NaI) detectors. NaI detectors are scintillation detectors. These detectors have a couple notable benefits. They have very high detection efficiency, and are very bright and are also comparatively cheap per unit volume. This allows for the creation of very large arrays like MTAS which was mentioned in Section 2.2.1. The brightness is a measure of how many photoelectrons per unit of incoming γ-ray energy (usually expressed as photons/MeV) the scintillator produces, with NaI being one of the brightest, as well as being cheap to manufacture in large volumes. The NaI detectors that were used with VANDLE (Seen in Figure 3.4) were manufactured by Saint-Gobain, and have an integrated PMT. These detectors are large, 2x4x16 in^3; which helps with their detection efficiency at higher energies. However, they have a stainless steel casing which gives them a higher than ideal threshold. These particular detectors were originally designed and optimized for portal monitor type applications where these two drawbacks are actually benefits; reducing low energy environmental noise and a robust casing to protect the NaI.

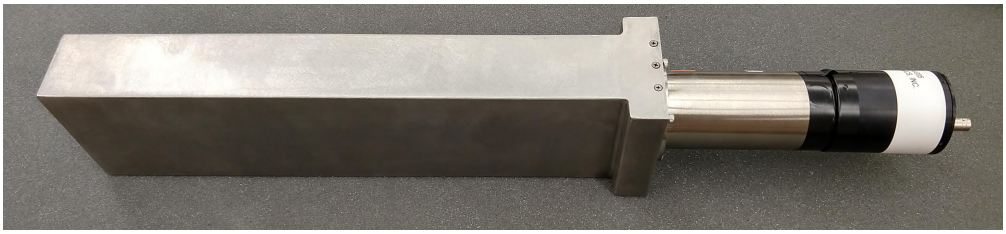


Figure 3.4: NaI detector used with VANDLE at the ORNL2016 and NSCL2016 experiments

3.3.3 Lanthanum Bromide

The lanthanum bromide ($LaBr_3$) detectors are a good compromise between the efficiency of the NaI and the resolution of the HPGe. The $LaBr_3$ detectors used in this work are from the Hybrid Array of Gamma-Ray Detectors (HAGRiD)[18]. The HARGiD detectors are BrilLanCe 380 crystals from Saint Gobain, and a picture of one used with VANDLE is seen in Figure 3.7. BrilLanCe380 crystals have the best energy resolution of any scintilator, while retaining a high intrinsic detection efficiency. These detectors have other benefits, such as a fast decay time and the linearity of the light response. All of these benefits make them good detectors to couple with VANDLE, but their disadvantage is the internal contamination. The HAGRiD crystals have internal contamination from Actinium-227 (Ac) which is an alpha emitter, and the unstable isotope Lanthanum-138 (La)[19].

The alphas from the ^{227}Ac contamination have energies between ∼1.6MeV and ∼2.7MeV [19], but this contamination is a smaller part of the background than the ^{138}La. These alphas are very close to the energies of prominent background γ-ray lines, in particular ^{208}Th (2.61 MeV) and ^{214}Bi (1.76 MeV). This causes some complications when trying to calibrate the energy response of the detectors, since it is hard to find a calibration source with a γ-ray line at those energies with sufficient intensity to be usable. The other source of contamination is the naturally occurring ^{138}La. This source is a much larger component of the background (See Figure 3.5). The ^{138}La has two decay modes, β^- and electron capture which were discussed in Chapter 1. The electron capture process gives a 1436 keV γ-ray and a few low-energy X-rays; while the β^-process emits a 789 keV γ-ray and a β particle with an end point energy of ∼255 keV. The 1436 keV γ-ray comes in coincidence with a Ba K-level X-ray; this leads to a summing effect and a resulting energy, as seen by the PMT, of 1473 keV. The 789

keV γ-ray gets smeared with the coincident β particle, leading to a continuum that ends around 1 MeV. Both of these are around the useful calibration lines of ^{40}K at 1441 keV and ^{60}Co at 1173 keV and 1332 keV lines. This means that a long background run is required for calibrations, and should be done around the same time as the source runs to minimize environmental shifts in the gain of the PMTs.

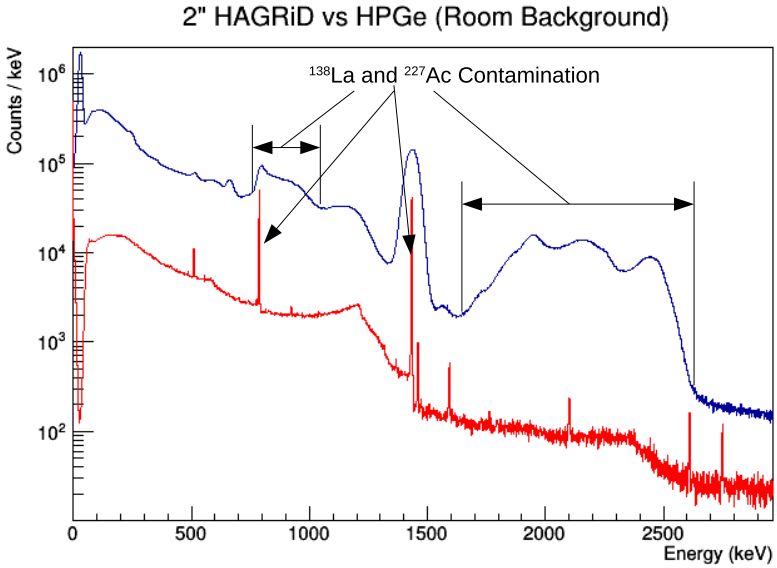


Figure 3.5: Experiment room background most of the counts are from the ^{138}La or ^{227}Ac. These data was taken over the course of about two days. The total of the sixteen HAGRiD detectors are shown in blue while the total of the four HPGe from the clover is in red

The other important impact of the contamination is in the determination of the efficiency. The various features of the background spectra interfere with evaluation of the peak to background area ratios. Shown in Figure 3.6 is a spectrum of a ^{137}Cs and a ^{60}Co source at the implantation point. These sources were designed for MTAS (2.2.1) and are therefore extremely weak, exacerbating the internal contamination problem. The ∼662 keV line from ^{137}Cs, while outside of the direct interference of the ^{138}La, is complicated by the the 789 keV line's Compton edge, and the same holds true for ^{60}Co's 1332 keV line and the 1436 keV ^{138}La line's edge. Whether its the 37 keV X-ray or the Compton edges of the two ^{138}La lines; this contamination is something to be very mindful of and future VANDLE experimenters will need to be careful when choosing calibration and efficiency sources.

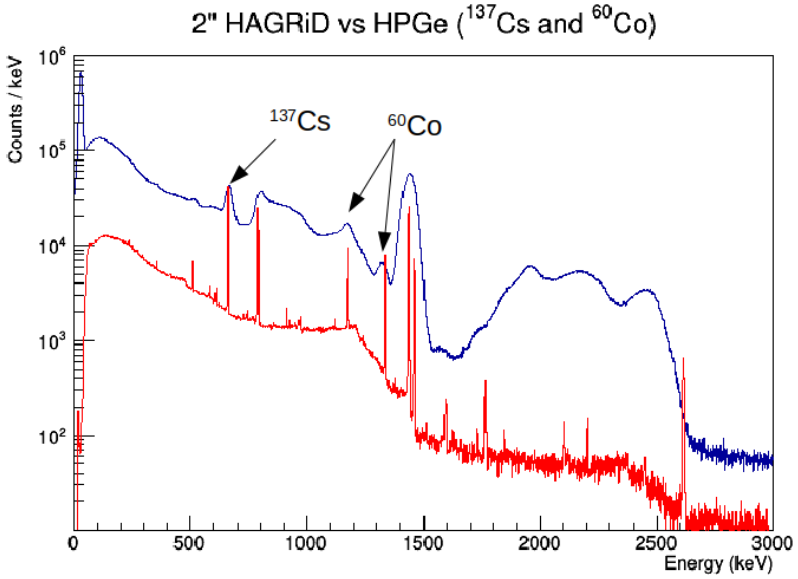


Figure 3.6: Spectra taken with ^{137}Cs and ^{60}Co sources. Again HAGRiD is shown in blue while the HPGe is in red

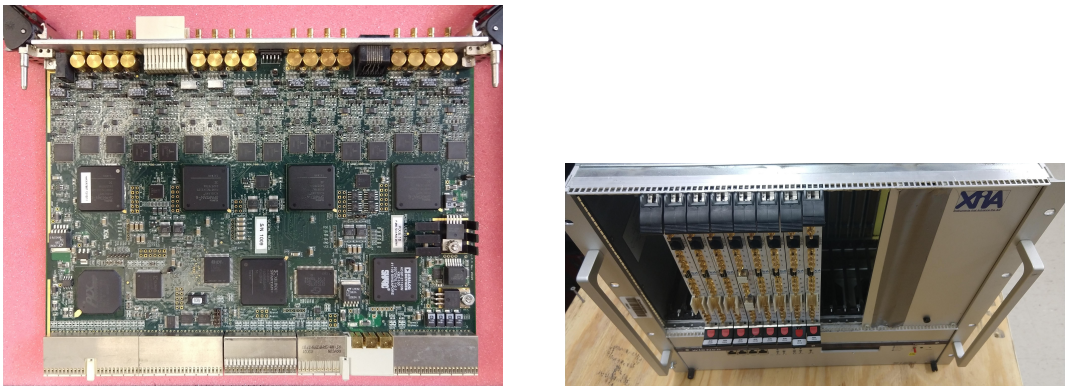


Figure 3.7: 2" HAGRiD ($LaBr_3$:Ce) used with VANDLE at the ORNL2016 and NSCL2016 experiments

3.4 Digital Data Acquisition System

VANDLE uses a fully digital system for data acquisition called Pixie produced by XIA LLC. This system gives enormous flexibility to couple VANDLE to external systems and maintain a singluar data stream. VANDLE uses the Pixie16 12 bit 250 megasamples per second (MS/s) variant of Pixie. These cards (see Figure 3.8a) have 16 channels, hence the name Pixie16. The 250 MHz gives a sampling period of 1 sample every 4 nanoseconds. By recording the full waveform of the incoming signal and fitting the leading edge during analysis we are able to get below the 4ns resolution of the pixie clock; around 1 ns for the γ

flash in VANDLE. This gamma flash comes from the γ-rays given off following a β decay, and since γ-rays have a constant velocity regardless of energy; they serve as a way to align the system in time. The bit resolution is a measure of how fine the binning of the height of the waveform is. For example 12 bit resolution gives 4096 (2^{12}) bins inside of the input range of the ADC. Increasing the bit resolution would give a more accurate measure of the amount of charge collected by the detector, this gives a more accurate insight to the energetics of the interaction. The sampling frequency is a little more self explanatory; a higher frequency means that the continuous waveform is discretized into more samples inside of a given length of time. A higher frequency gives more data points for the fit of the leading edge, as well as giving better timing for the elements of the setup that are not recording the waveform; due to data rate concerns or because the trace would not provide any extra benefit over the onboard filters. The 12 bit 250 MHz version of the boards were chosen because they provided the best performance per dollar when VANDLE was being designed. The timing was the subject of a long development process and the details of how we extract the timing from the trace are discussed in detail by Paulauskas *et al.* [20]



(a) **(b)**

Figure 3.8: Left: Pixie16 Rev F card. Right: Pixie Crate containing 8 Pixie16 Cards for 128 channels

3.5 Tape Transport System

The Tape Transport System is a critical component of VANDLE when running in ISOL facilities like Oak Ridge National Laboratory's former Holifield Radioactive Beam Facility

(5.2). This system consists of a continuous roll of the implantation tape, which is 1/2 inch magnetic data storage tape, and the tape drive and controller. The tape system allows us to implant short lived radioactive species, measure for a few half lives and remove the longer lived descendants from the array. The same system, with experiment specific changes to the turn-around, has served VANDLE at ISOL facilities since the first run in 2012. The tape drive was designed and constructed by our collaborator Ed Zganjar at LSU [21]. VANDLE generally uses around 300 ft of the implantation tape. This allows for a turn over time of a few hours. The long turn over time gives the implanted nuclei and their descendants time to decay down to isotopes with half-lives in region of the days. Additionally, it is unlikely that the distance between the β detector and the tape storage box will be an exact even multiple of the total tape length, meaning that it is unlikely that a used spot on the tape will return to the center of the β detector. After the implantation and measurement phases the tape drive pulls the hot spot into the shielded container that houses the drive mechanism. This mechanism is shown in Figure 3.9. This is to ensure that the decays of the descendants do not cause extra background in the detectors. The length of time that beam is implanted and the measured is tuned to the isotope being studied, to minimize the amount of contaminates, and the impact of the subsequent decays that are not actively being studied.

These settings are generally optimized for 3-5 of the parent's $t_{1/2}$ of beam on followed by 5-10 of the parent's $t_{1/2}$ worth of decay time, with the beam off, before moving the implantation spot away. For ^{94}Rb these settings were six seconds beam on, followed by nine seconds of beam off. Since ^{94}Rb and its daughter have 2.7 and 75 second half-lives respectively, there is very little contamination in the data. Unfortunately with the high statistics run of ^{97}Rb, incorrect moving tape collector settings were used. For ^{97}Rb, which has a $t_{1/2}$ of 150 ms; this would result in ∼500 ms of beam on with a similar beam off time to reduce the contamination from to the β-decay of ^{97}Sr, which has a 430 ms $t_{1/2}$. However, I was unaware that this particular run had a cycle of 3 seconds beam on and 3 seconds beam off which is 40 half-lives of ^{97}Rb and approximately 14 half-lives of ^{97}Sr in total. This results in a build up of both strontium and yttrium, rubidium's granddaughter, which contaminates the γ-ray spectra and makes the gating challenging. This should not affect the neutron spectra, other than the increased random background, since neither ^{97}Sr (P_n = 0.05%) or ^{97}Y (P_n

= 0.06%) have significant β_n decay branches. By restricting the analysis to the beginning of the tape cycle, it should be possible to cut out the contamination, while retaining the majority of the ^{97}Rb data. This is restriction requires a change to PAASS's ROOT TTree, and as such is still ongoing. Using another run of ^{97}Rb for the analysis gives only a fraction of the statistics.

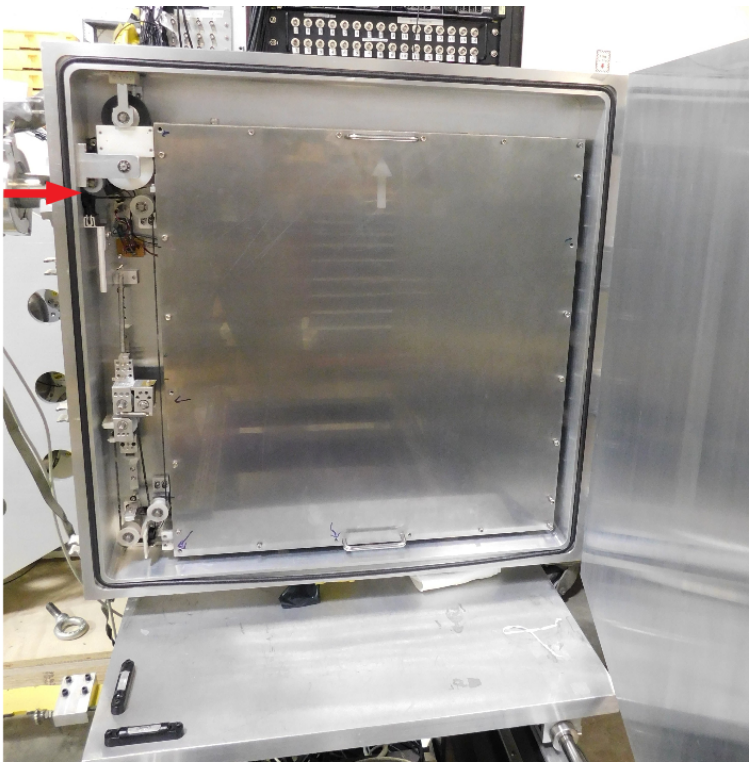


Figure 3.9: Picture of the inside of the shielded MTC drive. The tape enters near the arrow on the top left. The extra tape is stored in the square internal box, before going through the tensioning mechanism and then back to the implantation point through the same beam pipe it entered from.

3.6 PAASS

The Pixie Acquisition and Analysis Software Suite (PAASS) is the code suite that we use for data acquisition and analysis. It is an evolution of the group's former code bases, pixieSuite (for acquisition) and pixie_scan (for analysis). This code is designed to be as modular as possible, giving it the ability to be as flexible as the pixie acquisition system. The code is written mostly in C++; allowing it to be portable and easily expanded. PAASS handles

the unpacking of the data from binary file on disk, builds the events based on timestamps, and then passes the raw event to the various processors. This code uses an xml based configuration file which contains a list of processors that the user wants to use in the analysis, and then a map of channel specific information. This information lists the detector's type, and subtype; as well as parameters for channel-level calibrations, and the trace fitting. Channel-level calibrations include the ADC unit to energy calibration, and the trace fitting parameters [22].

Chapter 4

VANDLE's Evolution

4.1 Initial development

VANDLE's development started in 2008 with the initial design for the small and large bars [23]. During this time, before the first experiment, the timing and the intrinsic efficiency were determined and benchmarked. This development work was the subject of two Nuclear Instruments and Methods A papers. First was on one the development of the timing algorithm by Paulauskas *et al.* [20]. The second was by Peters *et al.*, which covers the development and characterization of VANDLE iteself. [24].

4.2 ORNL 2012 LERIBSS Campaign

VANDLE was first run at Oak Ridge National Laboratory's Hollifield Facility in 2012 at the Low Energy Radioactive Ion Beam Spectrography Station (LERIBSS). For this experiment the group used 48 small bars and 2 High Purity Germanium (HPGe) Clover detectors, as seen in Figure 4.1. The experiment was complicated by a large amount of neutron scattering from the heavy steel frame and the clovers themselves as well as the general characteristics of the experiment room; and from the low efficiency of the start detector. [8][25]

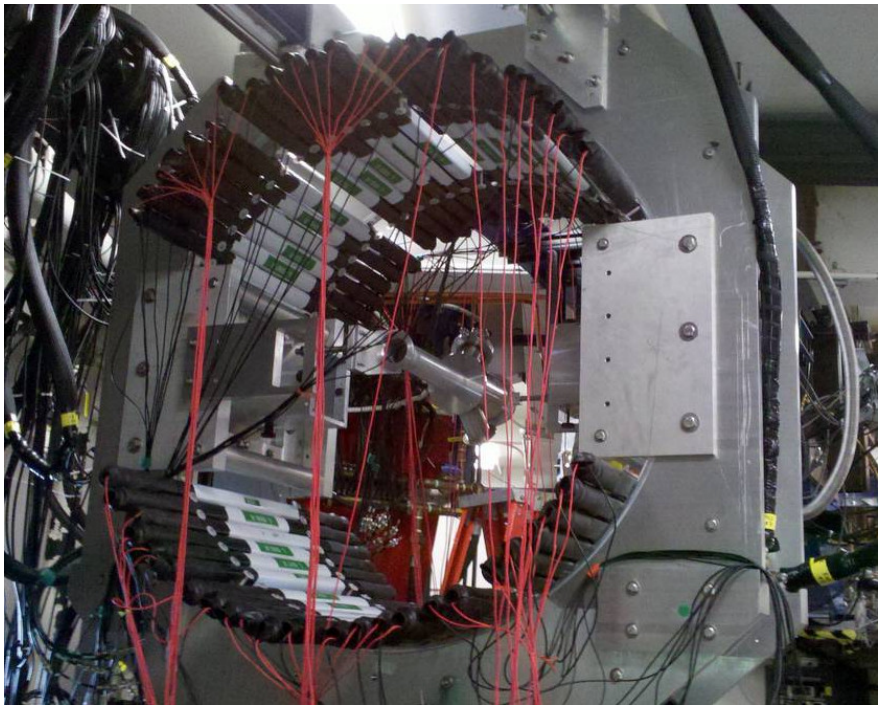


Figure 4.1: Original VANDLE setup at LERIBSS. Not pictured are the HPGe clovers but the mounts are visible to the left and right of the beampipe in the middle of the arcs

4.3 VANDLE Implementation at CARIBU (Argonne National Lab)

VANDLE was upgraded using the knowledge gained from the run at LERIBSS for the early 2015 run at Argonne National Laboratory's CAlifornium Rare Isotope Breeder Upgrade (CARIBU) source. The upgrades included the new bar size, the medium bar, and a new β detection system. The medium bars were designed to cover the same solid angle as the small bars with a 1 meter flight path, versus 50 cm. This gives better time resolution and subsequently better neutron energy resolution. The new β system utilized the new technology of Silicon Photo Multipliers (SiPM); these allowed for the β system to be placed inside the beampipe, in vacuum (Figure 4.2a). Two of the benefits of this, are the reduced threshold for detecting βs, and the increased efficiency due to the closer proximity to the implantation point. Another improvement was switching from single ended β detectors to a bar style, with a SiPM on the two ends of the β pad, similar to the VANDLE modules. As seen in

Figure 4.2b, the ANL frame still used 2 HPGe clovers but their position was changed to minimize neutron scattering off of the germanium itself and the aluminum housing. This was the start of the design philosophy used in subsequent frames, with VANDLE on top and the γ detection system underneath.

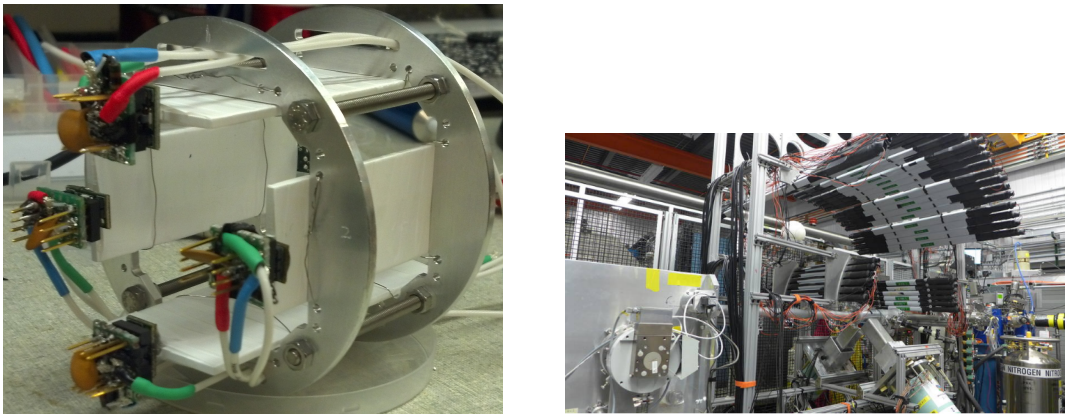


Figure 4.2: Left: New β detection system utilizing SiPMs. Right: Argonne National Laboratory configuration

4.4 CERN ISOLDE Decay Station

With these upgrades completed VANDLE was shipped to CERN's ISOLDE in the summer of 2015. Due to the dimensions of the room, specifically the height, a new frame was needed. This frame keeps the same design philosophy of the ANL configuration, but turns it 90 degrees (Figure 4.3). Leveraging the existing ISOLDE Decay Station (IDS), this setup used 2 HPGe clovers, and the existing 26 medium bars and 10 small bars. VANDLE preformed as expected, but the need for changes to the ISOLDE Decay Station beta chamber was identified. It suffered from similar problems to the LERIBSS frame, large amounts of high-Z materials close to the implantation spot and around the flight path in general. Upgrades to the chamber itself were delayed until the next Large Hadron Collider (LHC) shutdown. VANDLE preformed well enough to warrant a European version called the Isolde Decay Station Neutron Detector (IDSND) which is a direct clone of VANDLE, and utilizes the same digital data acquisition infrastructure which was originally developed for VANDLE.

The IDSND array has performed two additional experiments since the first VANDLE run at IDS, with the only changes being the addition of two more HPGe clovers for a total of ,four and the removal of the IDSND small bars. This was because of the geometry of the implant chamber, which does not have enough thinned aluminum for both the small and medium bars.



Figure 4.3: ISOLDE IDS setup from 2017.

4.5 ORNL 2016 OLTF

The ANL experiment was the commissioning run for the medium bars. They performed well enough that the decision was made to extend the original 26 bars to 42, to cover a full 180 degrees (Shown in Figure 4.4a). A need was identified for higher γ-ray efficiency, to increase the coincidence rate between VANDLE and the γ-ray detectors. This led to the addition of the large volume NaI and the HAGRiD [$LaBr_3$(Ce)] scintillation detectors. It was decided to use a jenga-like stacked arrangement (Seen in Figure 4.4b). This arrangement consisted of 10 NaI detectors, 16 HAGRiD detectors, and retained 1 HPGe clover. HAGRiD was a new array and was not fully implemented at the time this experiment ran. The array

was using extra PMTs that were optimized for VANDLE. As such, we expect that future implementations with these detectors will have better performance. The NaI detectors were stacked around the HPGe clover, which had the added benefit of providing some shielding, protecting it from the natural background. Finally the HAGRiD were placed in two groups of two and two groups of six. The groups of two fit under the beampipe in the space left by the top two NaI, while the groups of six were placed on top of those two NaI detectors. The HPGe clover was retained for beam identification purposes during the run as well as a fallback if the additions failed to work properly. The performance of the γ-ray detection system for this experiment will be discussed later. From preliminary analysis, the decision was made to keep the existing setup, both the 42 VANDLE medium bars and the Gamma System, for the E14060 run at the National Superconducting Cyclotron Laboratory (NSCL).

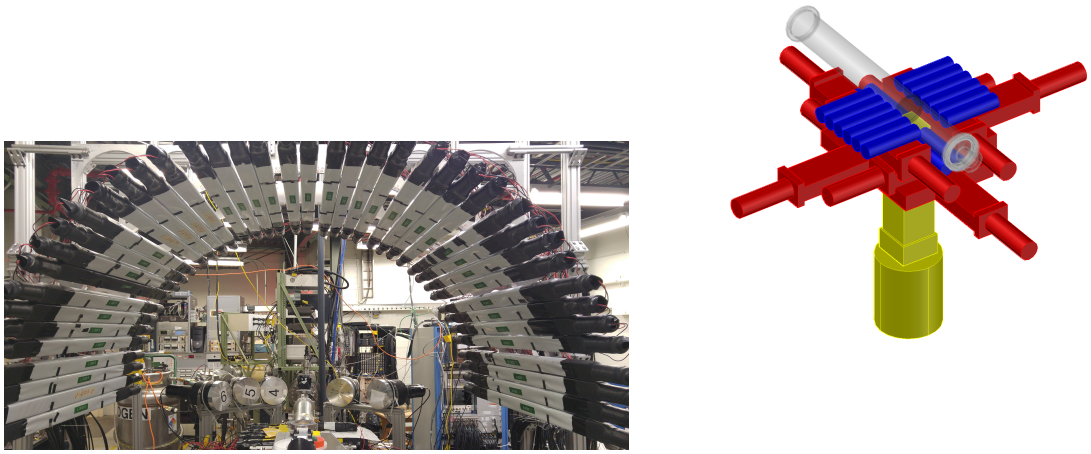


Figure 4.4: Left: Full Arc of Medium Bars as implemented at the OLTF in February of 2016. Right: Drawing of the new gamma-ray system. In yellow is the HPGe Clover, red is the NaI array, and blue are the 2" HAGRiD detectors. The beampipe is semi-transparent for clarity

4.6 2016 NSCL experiment (E14060)

The NSCL is a fragmentation facility and required the implementation of a position sensitive PMT for ion/decay correlations. This new implantation detector was the major upgrade for VANDLE in this experiment. Additionally the HAGRiD detectors were upgraded to optimized PMTs which offer better performance. The γ-ray detection system was supposed to remain the same with 1 HPGe clover, 10 NaI and 16 HAGRiD detectors; but a setup error caused the removal of the top 2 NaI detectors. Also it was decided that the 2 groups of two HAGRiD detectors situated under the beampipe would be shielded by the new implantation array so they were removed to reduce the count rate from the ^{138}La contamination. Seen in Figure 4.5 is the final arrangement of the γ-ray system for the NSCL run. The ease of configureing and re-configuring these detectors speaks to the power of fully modular setups like VANDLE and its ancillary systems.

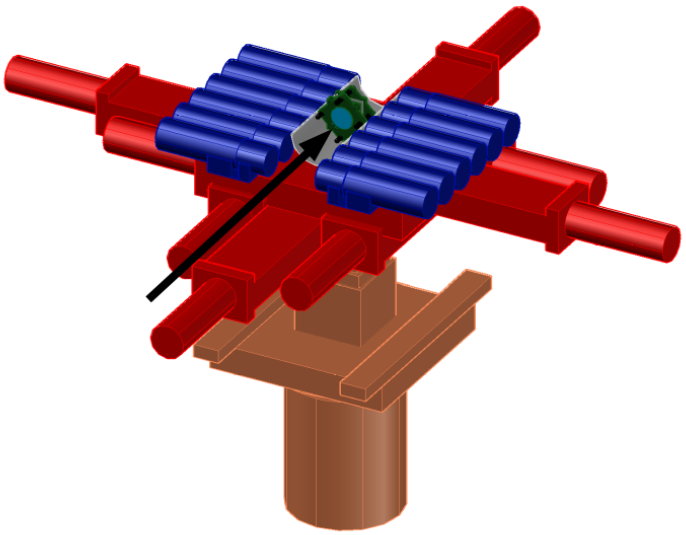


Figure 4.5: The γ-ray system as implemented at the NSCL in October 2016. The arrow indicates the beam direction. In the cut away of the beam pipe sits the PSPMT implantation detector. Here the HAGRiD are in blue, NaI in red, and the Clover is brown.

4.7 VANDLE at RIBF (RIKEN)

The next experiment for VANDLE will be in Japan at RIKEN in November 2018. This run requires a new frame due to the beam height at the setup location. The addition of the much larger 3" HAGRiD allows the full removal of the NaI for this experiment. This allows for a reduction in channel count while retaining most, if not all, of the efficiency due to the close packing. VANDLE is also getting a small upgrade to the clamp system that hold the bars in place, pushing the total bar count up to 48 on the 180 degree arc. The old mounting system (Figure 4.6a) used small C brackets to hold the bars, and were tightly packed in groups of four. By leveraging the 3D printing ability gained from the β systems starting with the ORNL version in 2016, a new mounting system was designed. The advantages of the new system is the loading order, and of course the increased bar count. By making the clamps hold both sides of the bars, we are able to load the bars on the arc from the middle out, which is easier and safer. As seen in Figure 4.6b, they allow for even spacing of the bars; therefore leading to the increase in bar count, and efficiency.

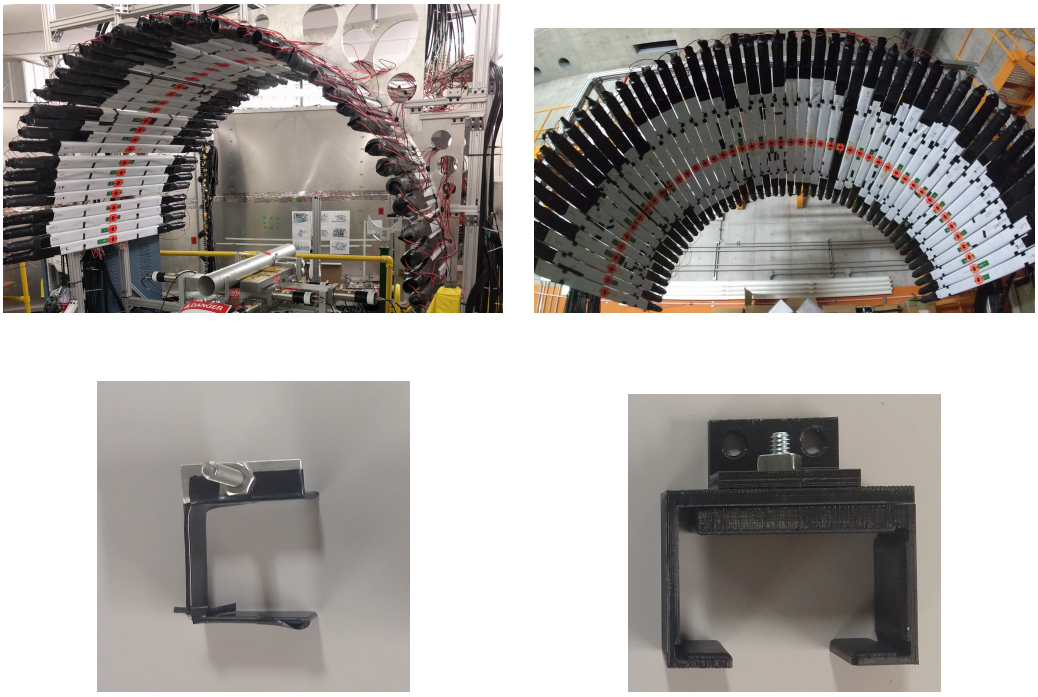


Figure 4.6: Left: Old medium bar support system. Right: New medium bar support system.

These new clamps required the design of new arc plates and ribs to hold them. The original design for the plates, used at the ANL experiment, was for a maximum of 26 bars. Extensions were designed for the OLTF experiment but the plates and the extensions had separate mounting points, which added complexity to the frame. By redesigning these we can simplify the assembly and alignment of the plates during experiment setup. The plates now attach to each other and require fewer connections to the overall frame to be supported. Additionally the upgrade of including rack mounting supports into the lower part of the frame allowing for the setup to be contained inside of a single footprint, helpful for small experiment locations. This upgrade is possible because of the height of the beamline at RIKEN's F11 location. A CAD render of the new frame can be seen in Figure 4.7.

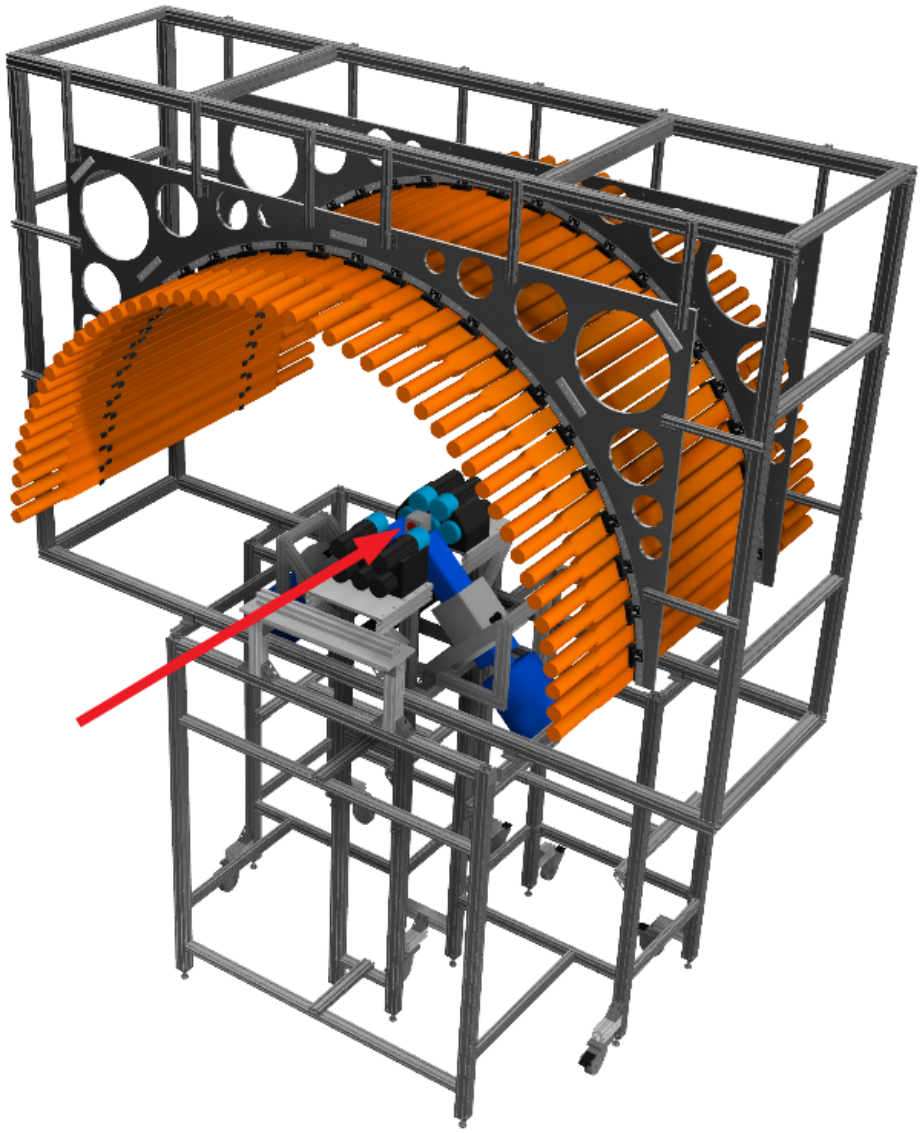


Figure 4.7: Isometric view of the new frame for RIKEN. Arrow represents the beam direction.

Chapter 5

Beta-delayed neutron spectroscopy of fission fragments at ORNL

5.1 Physics Justification

The ORNL experiment in 2016 aimed to perform β-delayed neutron spectroscopy of isotopic chains of rubidium, cesium, bromine and iodine. The reasons to study these isotopes include aspects of fundamental research in the form of nuclear structure, as well as applied science for reactor heat and reactor anti-neutrino phyiscs. This thesis focuses on the rubidium measurements. Neutron rich rubidium (Z=37, A¿87) isotopes are located midway between the Z=28 and Z=50 shell closures, and beyond the N=50 shell for neutrons. Previous experimental data of β-delayed γ rays and β-delayed neutrons from neutron-rich rubidium exists ([26],[27],[28], [29]). Gamow-Teller decays of neutron-rich spherical rubidium isotopes likely proceed through the $\nu g_{7/2}$ to $\pi g_{9/2}$ transformation. In the decay of ^{94}Rb the daughter (^{94}Sr) state with the highest feeding is the 2141 keV (21.4%) state, which is significantly below the $S_n$value of 6.8 MeV ([27]). With the majority of the decay strength going to low energy states, this significantly suppresses the β_n probability. However, deformation changes the picture. In Figure 1.2, we can see that for Z=37 the nuclei move from spherical to highly deformed. The deformation further increases the density of states, and can change the highest occupied levels as well as changing the selection rules for the decays. In the context of a deformed nucleus, the normal selection rules for allowed Gamow-Teller transitions will

change to the Alaga rules [30]. Using Nilsson asymptotic quantum numbers the standard Gamow-Teller rules are now expressed as $\Delta\Omega$=0 or $\pm$1, $\Delta\Lambda$=0, Δn_z=0 and ΔN=0 ([30]). The Nilsson diagram shown in Figure 5.1 shows how the deformation affects the decay properties. Previous work by Krumlinde *et al.* [1] discussed how the deformation affects the β decay strength function for rubidium, and makes a detailed comparison between the spherical and deformed cases. With the help of the QRPA model, they show how the deformation spreads and redistributes the β-decay strength function. This directly affects the neutron emission branching ratios and spectroscopy.

With respect to nuclear data, the isotopes measured are all produced in the fission of uranium. Because β_n emitters are a significant source of neutrons in nuclear reactors, they must be properly accounted for in reactor models. Beta-delayed neutron emission provides a source of neutrons that are spread in time and are important to maintain the stability of reactor criticality [31]. This data set will contribute high statistics gamma-neutron coincidence measurements for several nuclei. Reactor models need this input to properly account for delayed neutrons that contribute to the neutron flux in the reactor core. The neutron flux in the core is a parameter of life-cycle modeling of the various material components the systems are made of. The reactor decay heat during the shutdown process is released through the β decays of fission fragments. The energy and time distributions are essential to model the energy release during shutdown, which has obvious safety implications. In the context of the nuclei discussed in this work, ^{94}Rb will be of more use for expanding nuclear data since its structure is well understood. While, the deformed nuclei such as ^{97}Rb, will also be interesting from a nuclear structure point of view.

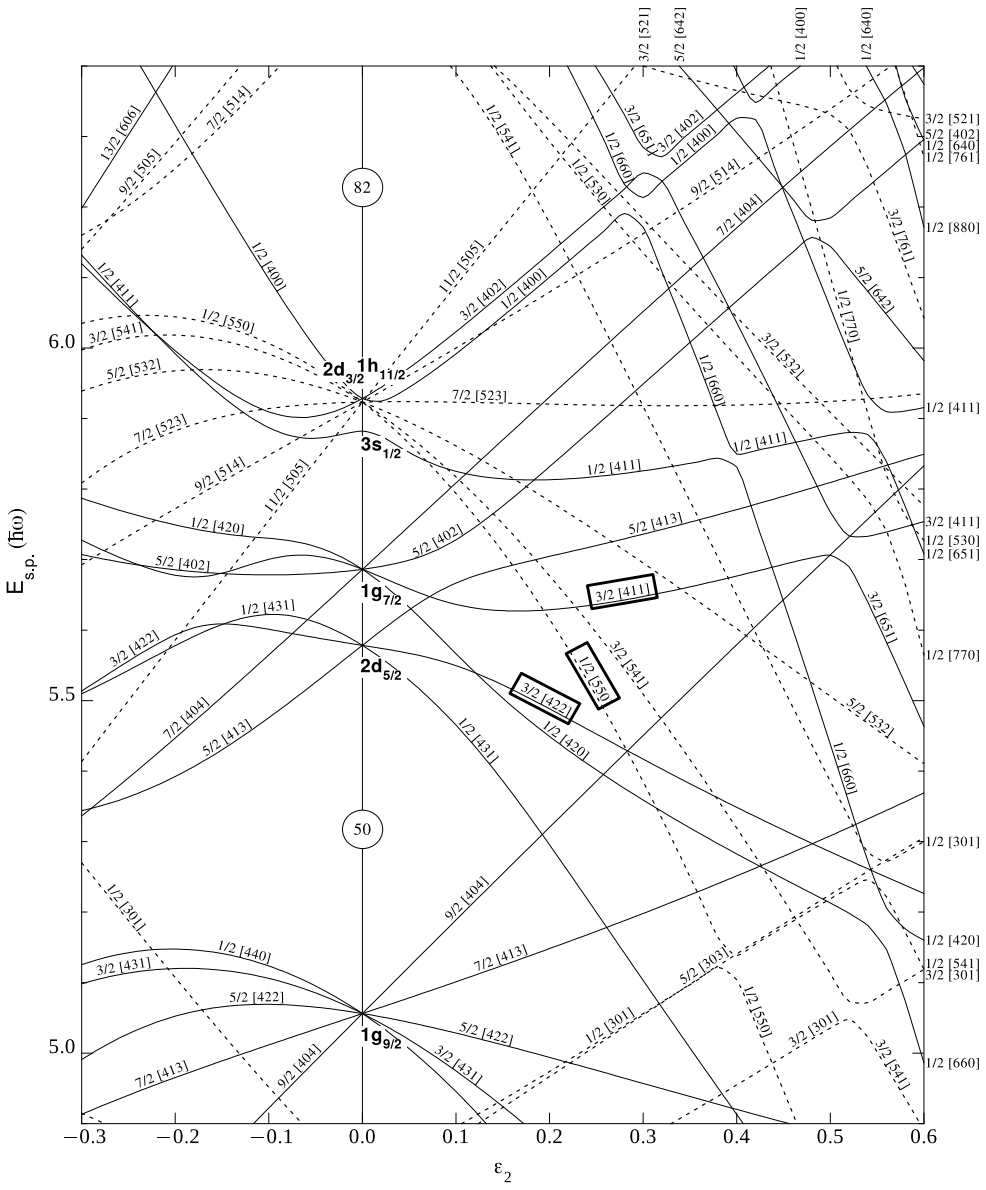


Figure 6. Nilsson diagram for neutrons, 50 ≤N ≤82 ($\varepsilon_4 = -\frac{2}{2}/6$).

Figure 5.1: Nilsson Diagram for 50 < N < 82. Marked are the active neutron orbitals near the Fermi energy for N=56.

5.2 Description of the Facility and Beam Production

This experiment took place at the Oak Ridge National Laboratory's Hollifield Radioactive Ion Beam Facility (HRIBF) in early 2016. HRIBF was an Isotope Separation On Line (ISOL) type facility. For this experiment the beam was created with 50 pnA of 38 MeV protons impinging on a uranium carbide (UCx) target at the On-Line Test Facility (OLTF), seen in Figure 5.2. The resulting induced fission produced the nuclei of interest. Seen in Figure 1.1 are the yields of different nuclei from uranium fission.

Due to the specific chemical properties of the nuclei, the ORNL Physics Division developed multiple types of ion sources to access the different fission products [32]. For this experiment the positive and negative surface ionization sources were used. The Uranium Carbide (UCx) target was heated by approximately 600 Amps (∼1700 °C) to help release the fragments from the UCx lattice. The fragments diffuse out of the target, into the ionization stage. For the positive source, the ionization surface is a tantalum tube with a heating current of about 250A; while the Negative source has a LaB_6 frit, a type of ceramic, at the end of an inert tube with the same heating current. The large electron affinity for tungsten, and the small ionization energy for LaB_6 ionizes the isotopes of interest. The fragments are accelerated out of the ionization stage by the several kV platform voltage. After some electrostatic focusing and deflection elements, the beam enters the dipole separation magnet. Due to the varying velocities of the different ionized fragment species we are able to separate them by varying the strength of the magnetic field so that the path of the ion of interest makes it through the 90° bend [32]. The now separated beam, goes through a few more electrostatic elements that focus the beam and deliver it to the experiment. Due to the limited resolution of the OLTF beamline there is always isobaric contamination of the beam. However for isotopes of rubidium and cesium these can be eliminated by adjustments to the temperature of both the target heater and the ionization surfaces. The contamination of neighboring masses can be eliminated by small adjustments to the dipole field, and the use of slits after the magnet to further minimize the acceptable paths for ions. In principle, the farther from the Alkali metals (Group 1) or Halogens (Group 17), depending on the ion source, the hotter the ionization surface needs to be to effectively ionize the element of

interest, which is the main reason why Rb and Cs can be made into reasonably pure beams. For the typical isobaric contaminates of Br and I the temperature of the ionization surface would have to be so high to effectively ionize Group 16 elements that the frit would melt, meaning that those beams are isobarically pure. Another factor influencing the beam rate is sublimation rate of the fission products in the UCx target; following a similar pattern as the ionization surface, the higher the heater temperature the better the release of the more chemically active fragments. The adjustments to the temperatures help direct the ion source yield of different elements. The fine control over the current in the separation dipole, and subsequently the field strength, along with the slits allow for good separation of the isobars. Having a highly focused beam allows the magnet and slits to be as effective as possible, because it minimizes the uncertainty in the starting points for the various paths through the magnetic field.

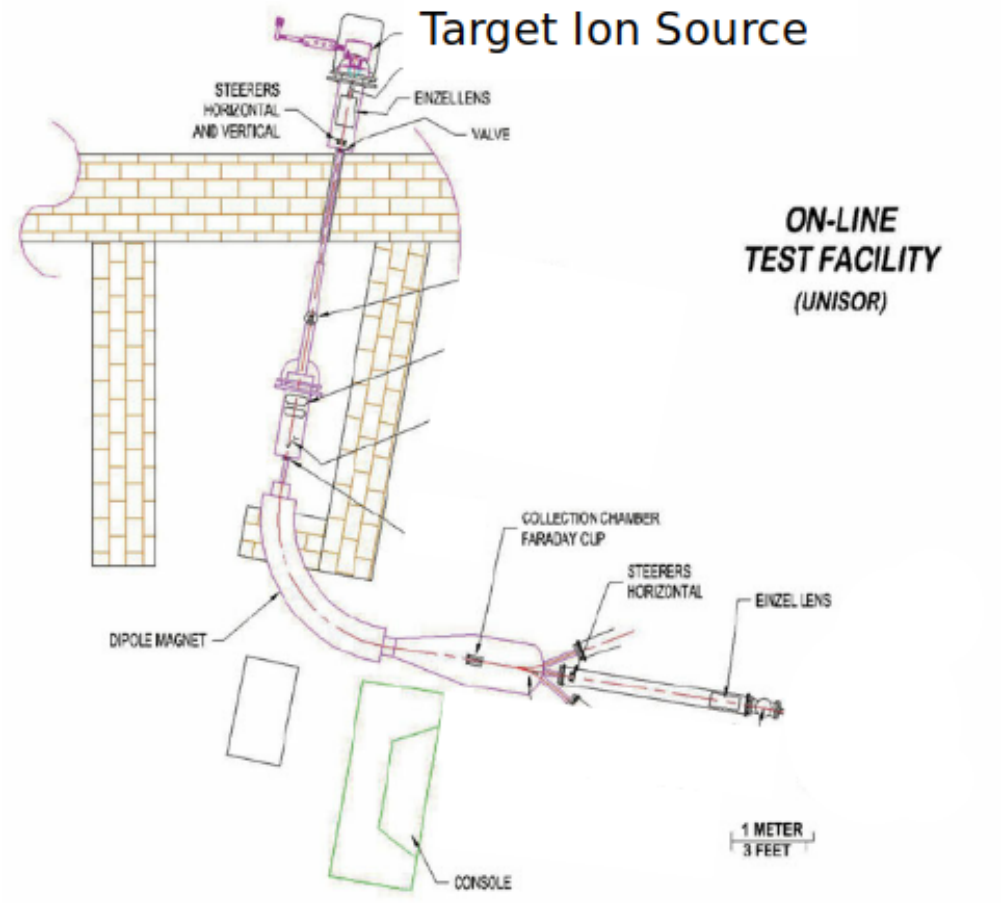


Figure 5.2: The On-Line Test Facility (OLTF) of the Holifield Radioactive Ion Beam Facility at Oak Ridge Nation Laboratory.

Chapter 6

Analysis Methods

6.1 Basic Analysis Methods of HAGRiD and VANDLE data

The basic methods for the analysis of HAGRiD and VANDLE data will be discussed here with more details in the specific sections later in this chapter. The analysis of the γ-ray detectors should lead to the reconstruction of a level-scheme based on γ-rays detected in coincidence with a β particle. The neutron-γ analysis should lead to neutron energy reconstruction; both in singles, and in coincidence with specific γ-rays.

6.1.1 Full Energy Reconstruction with HAGRiD and NaI

This is a new analysis method for VANDLE, since previously only low efficiency HPGe detectors were used. HAGRiD should have a much higher efficiency and should enable a calorimetry measurement, where the excitation energy of the γ-rays in a cascade can be reconstructed. The goal of this method is to try and reconstruct the full energy of the gamma decaying state, or at least catch the γ-rays that scatter from one detector to another and reconstruct the initial γ-ray energy. This is done by summing the energy registered in each detector together. However care must be taken to impose realistic constraints on time and geometry in this process. For high energy γ-ray reconstruction, the time difference

between successive interactions must be short, and it must be localized in the detector stack. A more specific explanation is in Section 7.1.1.

6.1.2 Analysis of Hybrid Data

This analysis method is the standard one used with VANDLE. This method involves gating on a specific event in one detector type and looking at what came in coincidence in the other detectors; for example gating on a specific γ-ray energy in either HAGRiD, or the clover and viewing the events in VANDLE or vice versa. Additional for specific detector types can be added, such as the time difference between the two ends of the VANDLE bar, or the time difference between the γ-ray and the nearest β detector event. These allow for the determination of time of flight spectra for a given γ-ray, or in reverse it allows for the identification of γ-rays that come in coincidence with a neutron event. Further explanation of this method is given in Sections 7.1.2 and 7.2.1. The full process of VANDLE's data analysis was described by Paulauskas *et al.* [25] and by Peters *et al.* [24]

6.2 Challenges

The experiments with β delayed neutron emission are very challenging. The ORNL experiment in 2016 had a few challenges not experienced before in a VANDLE analysis due to the addition of the γ-ray scintillators, the sheer volume of data, and one identified electronics misconfiguration error.

6.2.1 ^{138}La Contamination

As mentioned in Section 3.3.3, the HAGRiD detectors have internal contamination. This contamination comes from ^{138}La and from ^{227}Ac. The ^{227}Ac and its decay daughters produce an alpha particle background. However, these alpha particles do not have enough energy to be detected outside of the HAGRiD crystals themselves. Their energies are in the range of ∼1.6 MeV to ∼2.6 MeV. The ^{138}La isomer has a 10^{11} year half life, so it will not decrease over the life of the detectors. This isomer decays via electron capture (EC) and $\beta^-$with

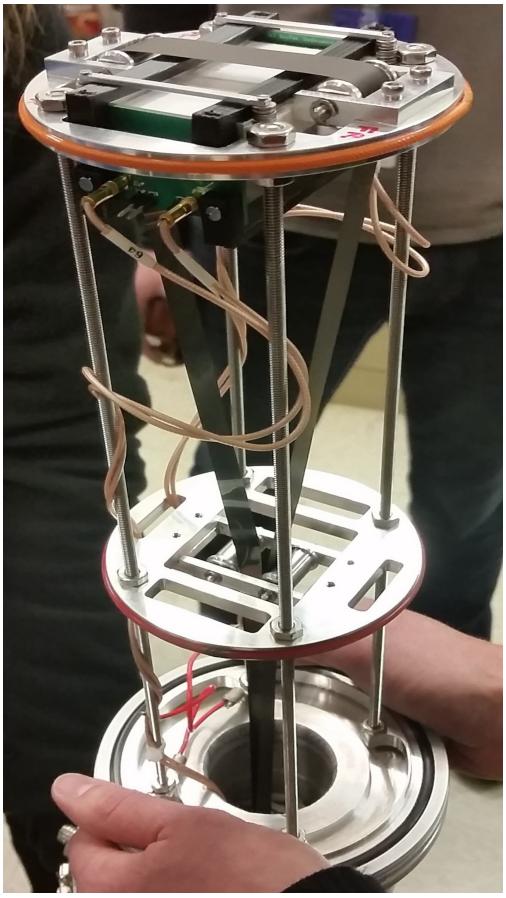
branching ratios of 66% and 33% respectively. The electron capture emits a 1438 keV γ-ray followed by X-rays from the daughter (^{138}Ba); while the β^-decay gives a 789 keV γ-ray and an electron with an end point of 255 keV. Both of these γ-rays introduce background into the other detectors in the setup; Figure 3.5 shows an example of this. While this background is significant, a simple gate on the β detector cuts most of the lanthanum contamination from the non-HAGRiD γ-ray detectors. The full effect of this background on the VANDLE modules is still being analyzed and is outside the scope of this thesis.

6.2.2 New Beta Detector

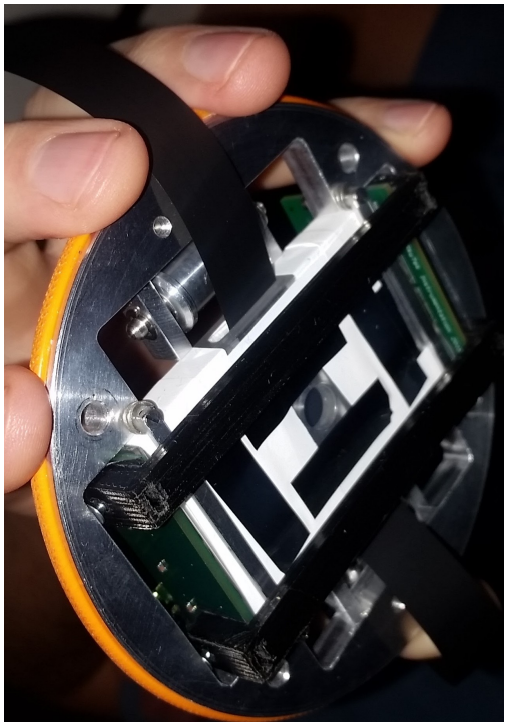
This experiment used our second generation β detector equipped with silicon photomultipliers (Figure 6.1). However, there were some problems. The beam from the OLTF could not be focused to be sufficiently small to fit though the small hole in the β detector's original plastic scintillator, seen in Figure 6.1b. This necessitated a change to a single solid block (6x4x0.6cm^3), located directly behind the implantation tape, which is shown in Figure 6.1a. This greatly reduced the solid angle coverage, resulting in a lowering of the detection efficiency. Shown in Figure 6.2 is the efficiency of the β detector as a function of the subsequent γ-ray seen in the clover. However, despite the loss of the efficiency, it was decided to continue the experiment with this detector. In addition, an artifact appeared in the VANDLE ToF vs QDC spectrum. By analyzing the wave forms of various detectors it was discovered that there were two problems with the β detectors used for the high-resolution timing. First, the traces had pile-up . Second, the trace delay was set incorrectly for the first Pixie module, as such, it was different from the rest of the modules. These two issues compounded in the PAASS's analysis of the waveforms. PAASS uses the maximum value in the trace to find the waveform. The pileup caused this to be misidentified, additionally the pileup changes shape of the waveform necessitating a change in the fitting parameters.

6.2.3 Large Data Volume

The data set was the largest to date taken with VANDLE, at ∼3TB of raw data. This was due to the use of more neutron detectors, the use of the HAGRiD and the long beam time



(a) β detector as used during the experiment in the mounting frame.



(b) Original β detector during assembly with the MTC tape running though a channel in the plastic scintillator.

Figure 6.1: Beta System for the 2016 ORNL experiment.

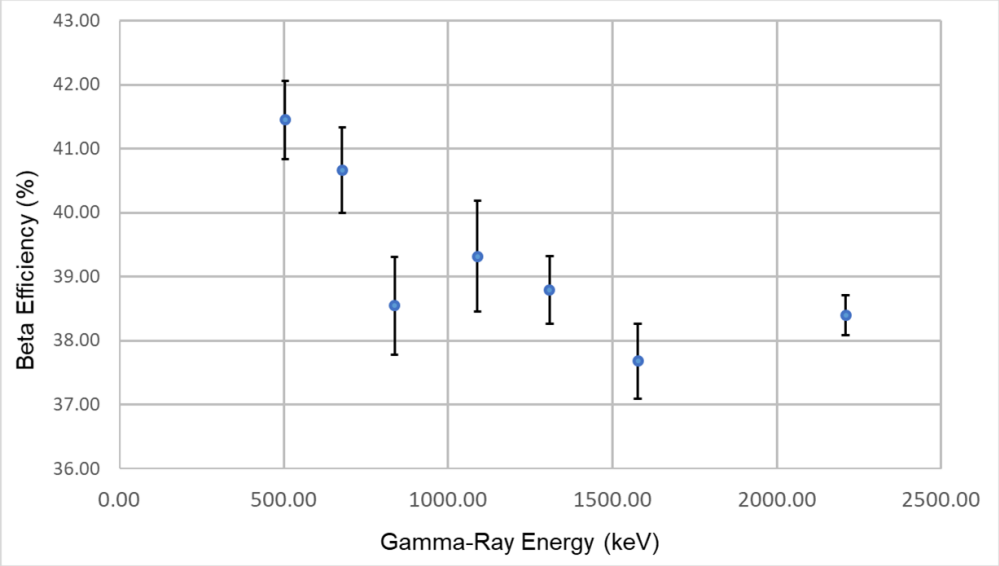


Figure 6.2: Efficiency of the β detector as a function of subsequent γ-ray energy as seen in the clover.

with abundantly produced isotopes . For example the ^{94}Rb run that will be discussed in Section 6.5, was taken in ∼8-10 hours with rates of several thousand ions per second, and has 200GB of raw data; while for the week long NSCL run in Oct 2016 only took ∼550GB of data was taken in total including calibration and setup runs. This data set exposed some deficiencies in how the analysis of experimental data is performed. The analysis code uses a rigid structure based on the ORNL libraries (ORPHAS) and visualization program (DAMM). In this analysis framework the histograms are rigidly defined. This makes sense for on-line data analysis but lacks flexibility for the off-line data manipulation. More complex gates would require re-running the PAASS code on the raw data again. Initially the scan of the 100 raw data files for ^{94}Rb would take about 2-2.5 weeks to complete. Even after code efficiency improvements, it still takes two to three days to scan the raw data files. Thus, PAASS is now used to mainly pre-process the data and the full off-line analysis is done in the ROOT analysis software suite [33]. Incorporating ROOT to replace some of the DAMM functionality provides the required efficiency and speed. By filling a ROOT tree with the processed data, like the calibrated energy of the detection event or the time of flight, cuts can be made dynamically and in a much shorter amount of time. Another advantage of this new scheme is that we can process each LDF with PAASS in parallel on on multi core computers,

and then add the outputs together to generate a single tree to make histograms from; this greatly speeds up the data processing time. This large data set also exposed the limitations of our computing hardware. With 56 cpu cores we run into the limit of the I/O bus of the server's hard drives; with the addition of new fast access solid state drives (NVMe SSD), we are able to take full advantage of the CPU cores. With these improvements the time to scan the ^{94}Rb data set down to 6 hours on 50 processing cores. From here the ROOT trees are run through a macro that generates a similar histogram list to what DAMM gives us, which only takes a few minutes when using PROOF, a component of the ROOT suite that enables parallel processing of ROOT trees. A more detailed explanation of the analysis is discussed later this chapter, in Section 6.5.

6.3 Detector Calibrations

6.3.1 HPGe Calibrations

As mentioned in Section 3.3, VANDLE has historically been coupled with HPGe detectors. One advantage of these detectors is the stability of the calibrations. This allows for the use of standard γ-ray sources to obtain the calibrations, we used ^{60}Co, ^{137}Cs, ^{133}Ba, as well as natural background lines from ^{214}Bs, and ^{208}Th. These give several energy calibration points from 80 keV from, ^{133}Ba, up to 2.6 MeV, from ^{208}Th; allowing for a robust energy calibration. A non linearity was discovered in the response of the clover during the analysis of ^{94}Rb. This required two calibration functions for each clover channel. The calibration functions were generated from ^{94}Rb data because it was already being implemented for the scintillators and spread of known lines in ^{94}Rb provide more calibration points at high energy. The calibrator would switch functions at 1 MeV as there were equal number of calibration points above and below this energy. Further, investigations deemed a change of the switching location to be unnecessary. The calibration functions are both linear, and have very similar slopes, but the intercepts are different. These nonlinearities are a small effect but because of the high resolution of the HPGe detectors, it is still noticeable. In Figure 6.3, we see the 1577 keV γ-ray which is a beta -delayed gamma from ^{94}Rb. With only a single calibration function

this peak is located at just over ∼1580 keV. Because of the use of two functions, there exists a possibility of a discontinuity at the boundary. The discontinuity was found to be less than 0.6 keV, and without a peak right around 1 MeV, this was marked as just something to be aware of.

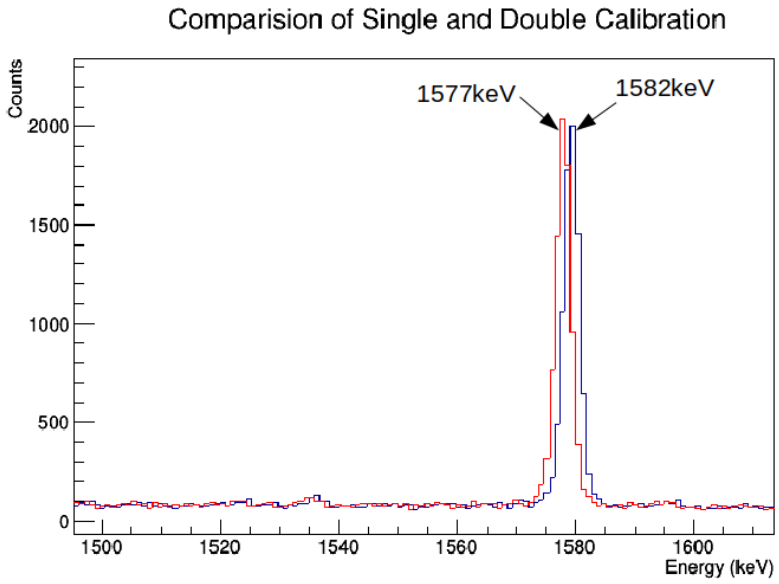


Figure 6.3: Comparison of 1577 keV γ-ray from ^{94}Rb calibrated with 1 or 2 functions. Red is with two functions, blue is with a single function.

6.3.2 Scintillators

The two scintillation detector types, however, showed operational instabilities. The HAGRiD and NaI detectors have large drifts in their calibrations, primarily coming from changes in the room temperature, and from the PMT's count rate. These drifts are a source of complication in data analysis, and necessitate internal data calibrations. As can be seen in Figure 6.4 the effect of the miscalibration gets larger as we move up in energy. Notice the peak just over ∼1400 keV. The internal data calibrations must also account for the drifts coming from the room temperature, meaning that a single data run might require multiple calibrations. Luckily, most facilities have enough control over the room temperature that this effect is minimized, and changes are seen on a time scale of days. For the ^{94}Rb data set, discussed later in this Chapter (Section 6.5), a single calibration is used even though the run was several hours in length.

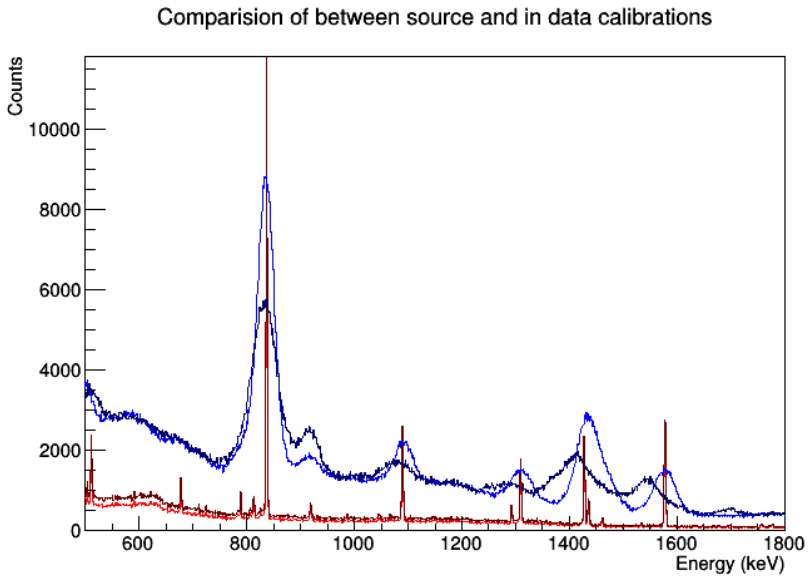


Figure 6.4: Comparison of ^{94}Rb data calibrated by sources and with internal calibrations. The red and burgundy lines are the HPGe data. The blue lines are the HAGRiD data; light blue is the in-data calibration and dark blue is using only source data for calibration

Internal data calibration can be difficult, which is exacerbated by the lower resolution of the HAGRiD and the NaI detectors (∼3% and ∼10% at 1MeV respectively). The lower resolution at smears the peaks together preventing them from being used for the calibrations. In the HAGRiD detectors, this prevents the use of ^{40}K, ^{217}Bi, and ^{208}Th as calibration sources because their γ-ray lines (1.46 MeV, 1.77 MeV and 2.6 MeV respectively) are too close to the internal background to be distinguished. For the NaI detectors, the layering of the detector system, seen in Figure 6.5, creates complications. The upper layers of NaI absorb the vast majority of the γ-rays coming from the beam, or the calibration sources. As a result, the lowest layer of the NaI stack sees mostly room background. For the lower layer, two transitions were used to generate the calibration, one from ^{94}Rb and one from the ^{208}Th background. The line from ^{94}Rb that was chosen was the very intense 836 keV transition. For the other layers, we had to use the same line from ^{94}Rb but we could not use the background line and instead were forced to use another line from ^{94}Rb. This second transition, at 1089 keV, is unfortunately very close to the first calibration point. This leads to a fragile calibration across the energy spectrum, requiring careful checking against existing data.

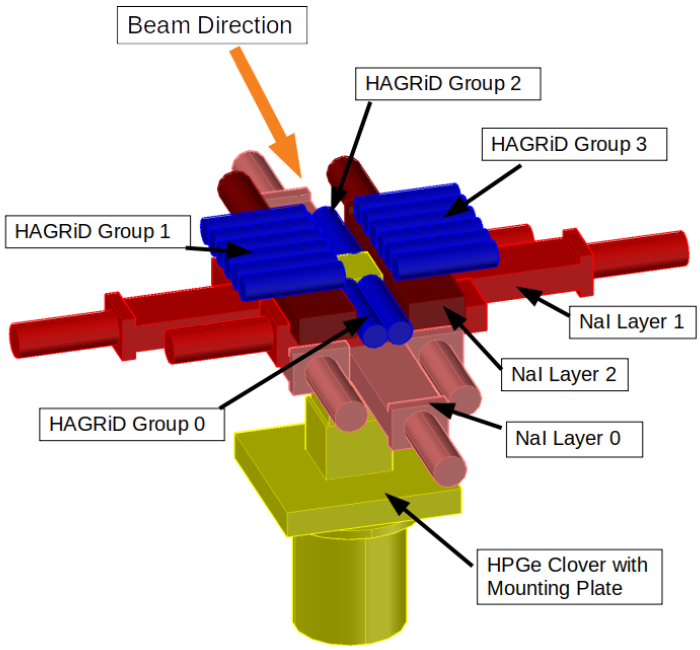


Figure 6.5: CAD render of the γ-ray detector stack with group labels.

6.4 Gamma-Ray Efficiency

After the calibration the next step in the analysis was to get the efficiency for the various γ-ray subsystems. The efficiency is measured with a calibrated source. These sources are calibrated with known efficiency HPGe detectors. For this experiment we used a mixed europium source, which contained ^{152,154,155}Eu. Because this is a mixed source it increases the density of the low energy lines making it hard to use with the low resolution detectors. Luckily, we also had calibrated ^{137}Cs, ^{60}Co, and ^{133}Ba sources. By utilizing all four sources, and selectively choosing single lines, it was possible to get the efficiency curves for the various detector systems. Unfortunately, the lowest layer of the NaI detectors (detectors numbered 0-3) did not see enough of the sources to be measured; and as such they were dropped from later analysis steps. Figure 6.6 is the full efficiency for the three subsystems, and the efficiency curves for the individual Clover, HAGRiD, and NaI detectors are shown in Figure 6.6. The Clover and HAGRiD curves look as expected from past measurements. The NaI, however, do not look as expected. Firstly, this is caused by the geometry of the γ-ray system as a whole, the NaI are shielded by the HAGRiD and/or the Clover. Secondly, since the NaI detectors are encased in steel which introduces a threshold effect due to the absorption of

low energy γ-rays by the steel, there is a decreased efficiency for low-energy γ-rays. To first order, previous VANDLE measurements had an efficiency for the HPGe detectors that was twice as large as this experiment, but that is the total γ-ray efficiency for those systems. For this experiment the total γ-ray efficiency increased significantly due to the addition of the HAGRiD and NaI detectors.

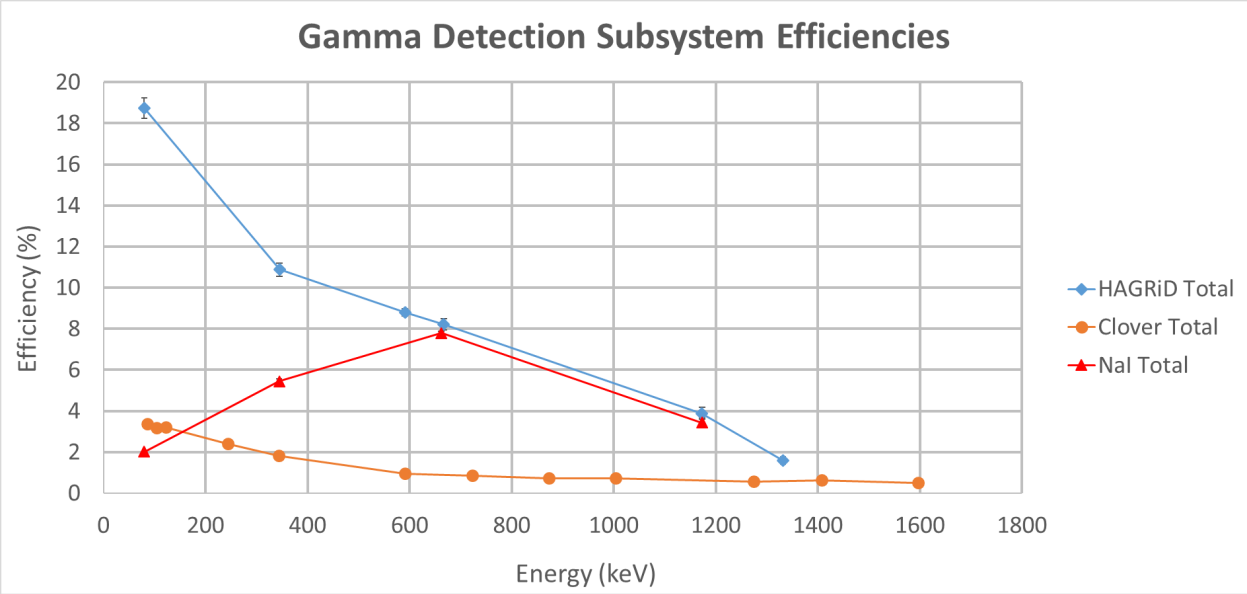
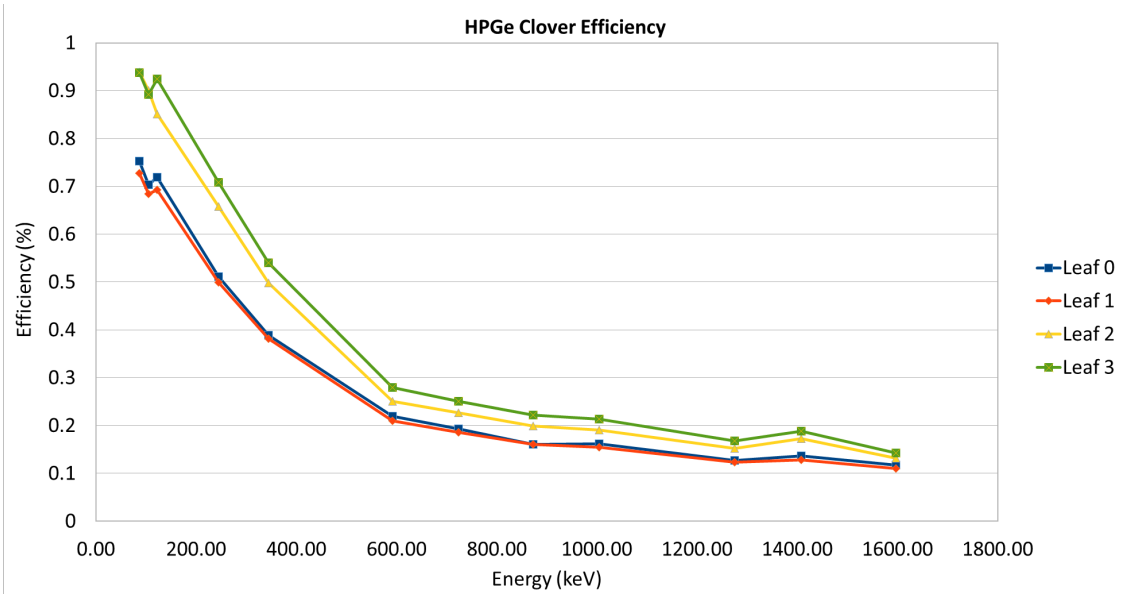


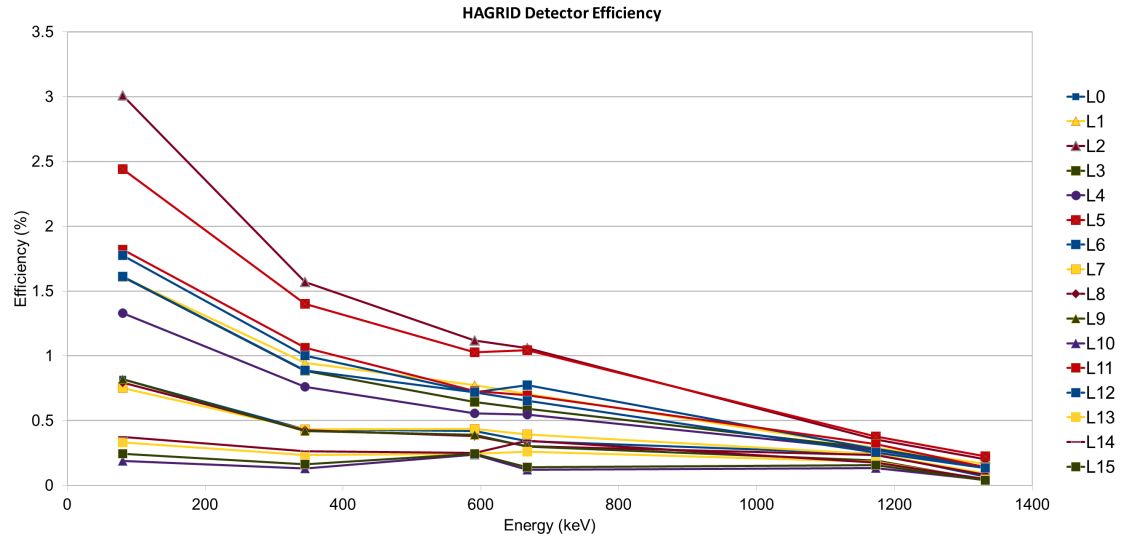
Figure 6.6: Efficiency curves for the three different subsystems of the γ-ray array

6.5 Analysis of hybrid data from HAGRID and VANDLE

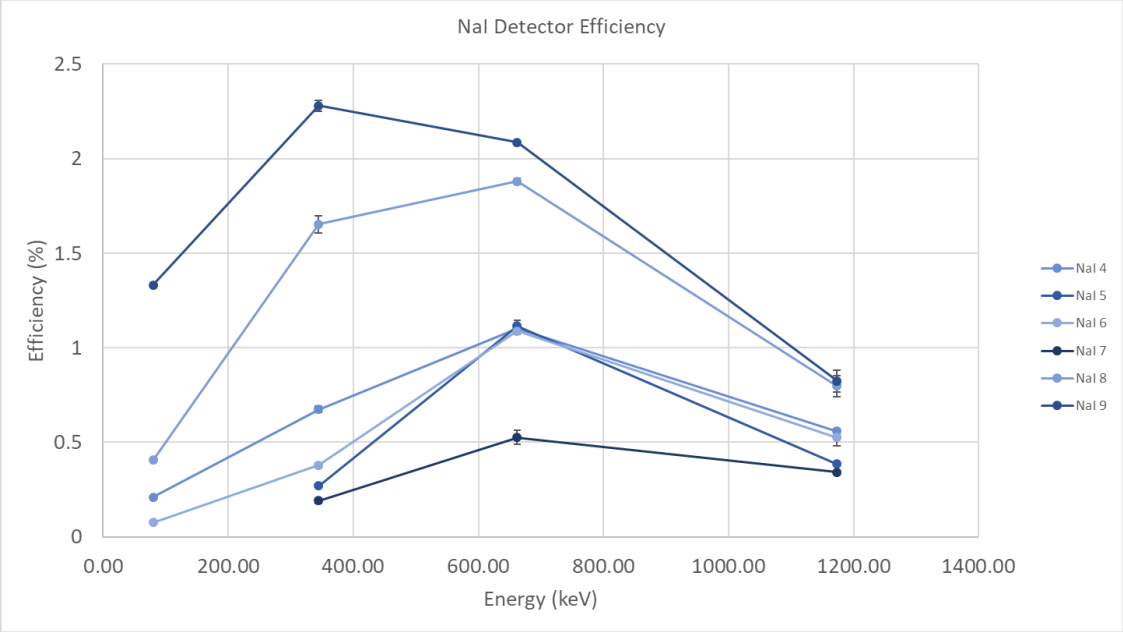
Hybrid arrays, like VANDLE, are designed for coincidence measurements. The data analysis relied on the software event builder in PAASS. These raw events are passed to the various detector type processors in PAASS. This code processes the data and return values of interest such as the Time of Flight for VANDLE events, or the time difference between the γ-ray and the β in nanoseconds rather than clock ticks of the pixie card. Once these structures are returned the ROOT tree is filled. This happens only once per pixie event, ensuring that events which are correlated remain correlated in the ROOT tree output. Currently this analysis has be focused on verification of existing data, before moving on to more exotic



(a) Efficiency curve for each leaf of the clover



(b) Efficiency curve for each HARGiD detector



(c) Efficiency curve for each NaI detector

Figure 6.6: Efficiency curves for the various types of γ-ray detector systems

isotopes. As such this analysis is broken into two parts. First is the development of a summing analysis for high-energy γ-rays, and second is the hybrid gating, which is the typical VANDLE procedure.

6.5.1 Full Energy Reconstruction

Higher energy γ-rays do not always deposit their full energy in a single interaction inside of the detector. They can and often do scatter via lots of small interactions. If all of these smaller interactions are inside of a single detection volume then the event will give the full energy of the γ-ray; due to that fact that the interactions are all extremely close in time, leading to a single signal from the PMT. However, if the photon leaves the detection volume, only a partial energy will be recorded. To correct for this we add back the energies in the event to recreate the initial γ-ray energy. In practice, one must be careful to impose realistic conditions to this addition. Generally, this is a time window outside of which we take any signals to be a new primary γ-ray. In the case of VANDLE's γ-system, spatial considerations must also be taken. For instance in HAGRiD, we should not sum signals that come from different groups that are separated by a large distance. For example, we should not sum

events in HAGRiD detector number 0, which is in group 0, with HAGRiD detector number 7, which is the upstream most detector in the group 1. This is because there is simply too much material in the way for a γ-ray to scatter that far undetected. For simplicity we have decided to preform the summing inside of the various groups (Figure 6.5) as a first pass for the analysis. These calculations are carried out using a ROOT TSelector, which allows for modifications to account for different spatial geometries, as well as to investigate the affects of the time and space windows, without reprocessing the raw data through PAASS.

6.5.2 Neutron Calibration and n-γ Analysis

Complete VANDLE data analysis requires proper neutron-γ coincidences. The goal is to construct neutron time of flight spectra in coincidence with specific γ-rays. It allows for proper reconstruction of the emitter's level structure. It also gives the energy partitioning; knowing how much energy goes into neutrons versus γ-rays versis β particles for the decay, which is important for the modeling of the decay heat. Implementaion of this method starts with time aligning the neutron detectors. For this, the prompt gamma rays are used. They have a known time of flight, regardless of energy, given by the speed of light. This allows us to calculate time zero for the decay using the measured distance from the implantation point to each individual VANDLE bar as well as the offset along the beam axis, if relevant. Next different cuts on QDC are taken to account for the low amplitude timing walk (see [20] for more information of the timing walk, as well as correction techniques). The time of flight versus the VANDLE bar number, before and after the time alignment, is shown in Figure 6.7.

Cuts and conditions must be imposed to clean up the data from uncorrelated events and background. These cuts include a projection on the time difference between the two ends of a VANDLE bar, as well as the time difference between the γ-ray and its correlated β. These time differences are driven by the physical orientation and dimensions of the detectors themselves. For example, the speed of light inside of a VANDLE bar is known; therefore we can cut out those randomly correlated events whose time difference would put the interaction outside of the physical detection volume. Care must be taken with the γ-β time cut because some γ-ray detectors have poor timing resolution (i.e. the clover). This

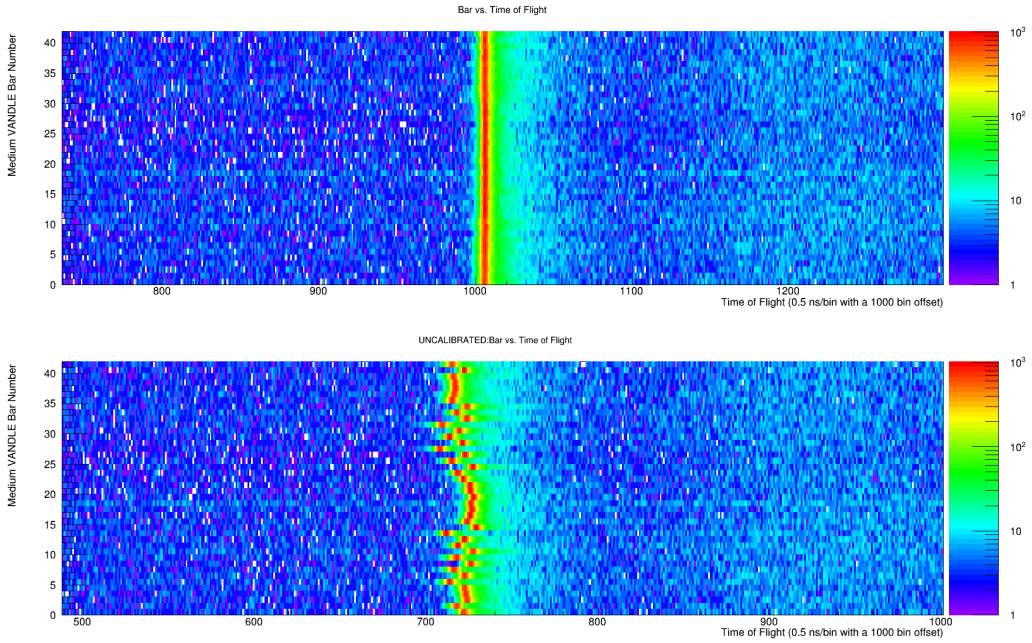


Figure 6.7: Top: Bar vs Time of Flight after alignment. Below: Bar vs Time of Flight before alignment

is one of the advantages of HAGRiD; $LaBr_3$ has excellent time resolution [19], and even without the high-resolution timing analysis, it can be seen in Figure 6.8 that the uncertainty in the time difference is much lower with the HAGRiD than with the clover.

The next step is to plot the time-of-flight versus the QDC for gates on specific γ-rays. We have observed a direct dependency between the time-of-flight resolution and the QDC deposited. As such, cuts on the QDC, and thus indirectly on neutron energy, are used to give the spectrum deconvolution code some initial conditions and bounds, which greatly increase the likelihood that the deconvolution procedure will be successful. VANDLE generally has a threshold of $\sim$100 keV neutrons, although this is dependent on the particular setup and environment of the experiment.

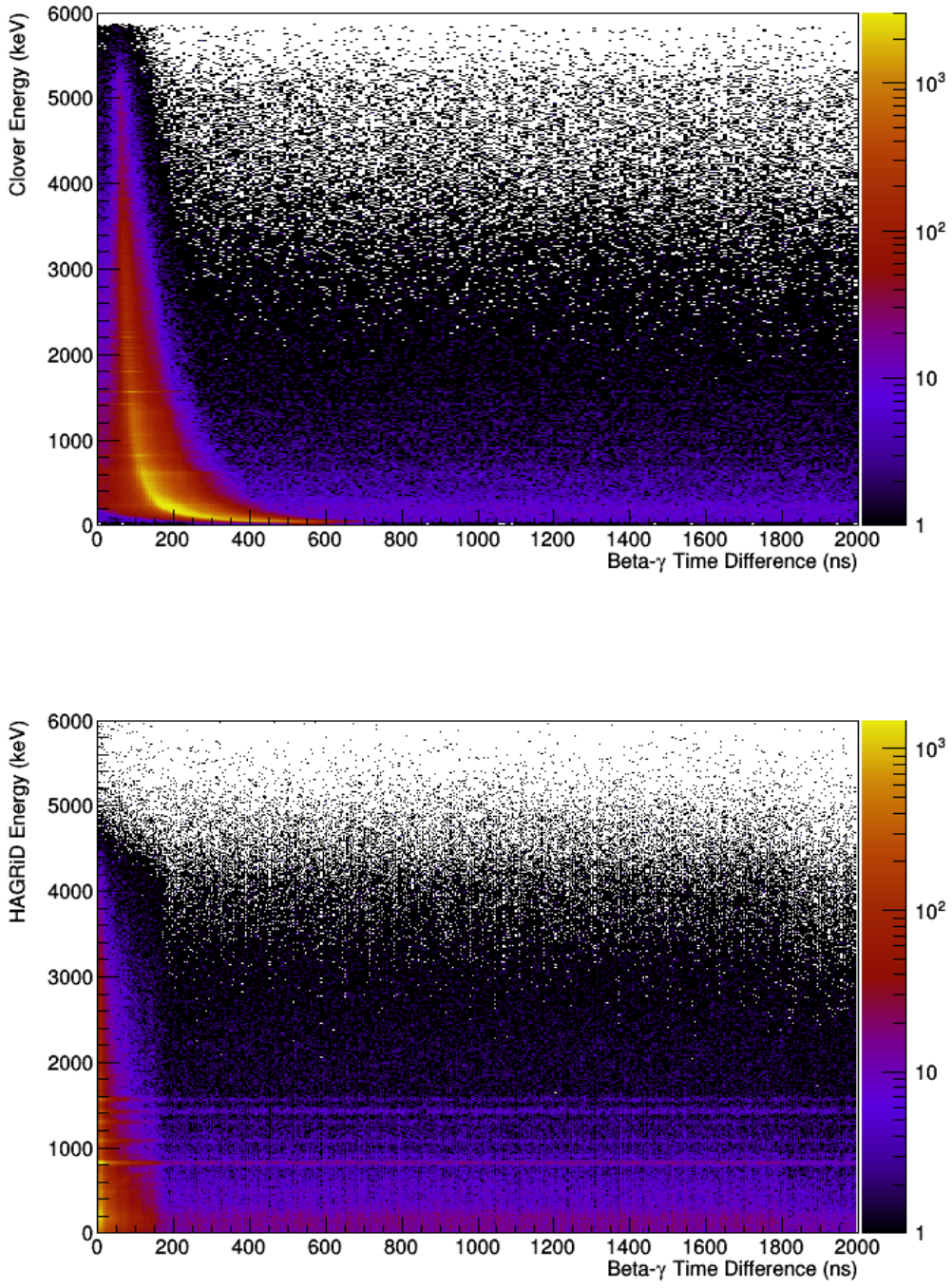


Figure 6.8: Upper: Clover energy vs β-γ time difference. Lower: HAGRiD energy vs β-γ time difference

Chapter 7

Results of Full Energy Reconstruction and Hybrid Analysis

Since both ^{94}Rb and ^{97}Rb have been measured previously; it gives us the ability to cross check our results. As mentioned previously, (Section: 5.1), Rubidium isotopes and their decay daughter, Strontium, are the quintessential mid-shell nuclei, and the heavier isotopes are highly deformed. Being mid-shell the level density is very high, resulting in a large number of potential decay paths. This can be seen in the data from the clover (Figure 7.1) where we have a large number of lines that survive a gate on the β detector. Both of the two nuclei that are used in this work were studied in the late 1970's and 1980's. We will compare to work completed by Brady *et al.* [26]. Ion-chamber 3He based detectors can be run in proportional mode, so that the energy information is retained. These detectors offer excellent neutron resolution and good efficiency for low energies but at around 1 MeV the efficiency becomes very small. They did not make a coincidence measurement. We hope to expand their measurements by offering neutron-γ coincidences as well as better efficiency for higher energy neutrons. Attached to the results figures are the results from Brady *et al.* in both neutron energy and an expected time-of-flight spectrum.

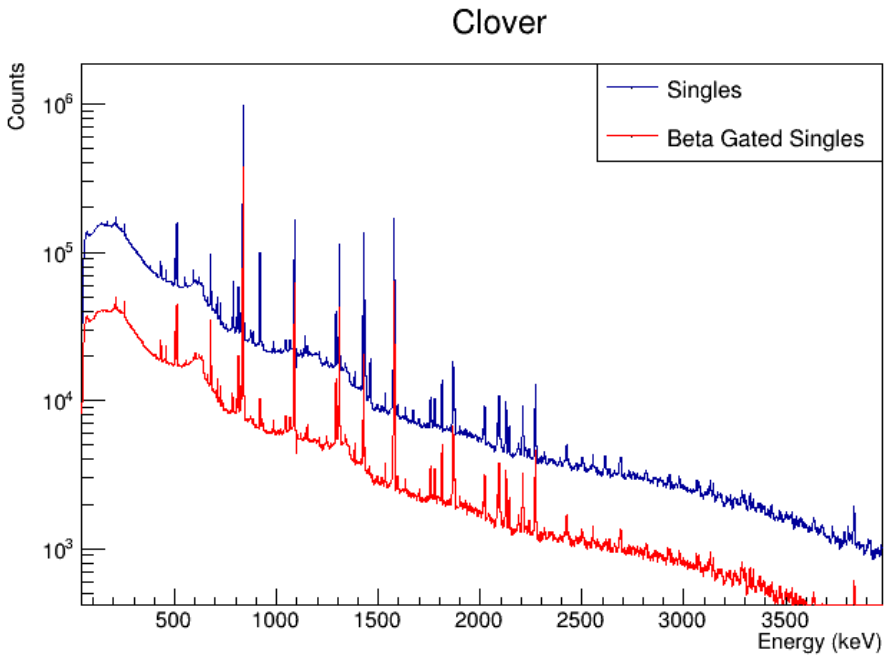


Figure 7.1: Clover singles vs β-gated singles in ^{94}Rb

7.1 ^{94}Rb

7.1.1 Full Energy Reconstruction

The figures below show the reconstructed the level excitation scheme for several states of ^{94}Sr. We still see single γ-rays in the total energy seen by all γ-ray detectors. This is caused by the finite γ-ray efficiency; meaning that part of the cascade was just missed by the system. A γ-ray could scatter off of one of the HAGRiDs into the clover, or one of the top two layers of NaI, but this step would require an analysis with a unified resolution for the different detector types. That was decided to be outside of the scope of this analysis, but is a possible step for future analyses if needed. The next goal for this part of the analysis is to look for high energy γ-rays or low-lying levels that come with neutrons.

Shown in Figure 7.3 is a partial level scheme for ^{94}Rb, showing the states below 3 MeV. In Figure 7.2 I have plotted the γ-rays seen in the clover detector verses the total energy seen by the whole γ-ray system. This spectrum shows single γ-rays in the clover on the X axis and the total event energy on the Y axis. The vertical line near the middle of the X axis is the 1577 keV γ-ray; the hot spot shows the original level energy. By projecting that spectra

onto the event energy axis; it should be possible to see how much energy was deposited into the γ-ray system for events where the clover saw that particular γ-ray. Projections of this spectra, seen in Figure 7.4, should indicate the level that initially decayed, but the lack of efficiency makes this challenging for states with low intensity lines or for cascades with a high multiplicy. However, as mentioned earlier, this is a high statistics measurement of ^{94}Rb. Projections are gated on known γ-rays from ^{94}Rb. These levels have I_β ranging from 1.28% for the 2965 keV level to 21.4%, for the 2414 keV level and have similar γ-ray intensities [27]. These projections show that it is possible for us to reconstruct the levels for low multiplicity cascades even for weak feedings, given enough statistics. Of note is Figure 7.4b, which depicts the 2146 keV level from the 1309 keV γ-ray. In that figure we see the 2146 keV level, but we also see a hint of the the 2603 keV level which feeds into the 2146 keV level with an I_β of 1.4% and only de-excited through the 2146 keV level 0.39% of the time.

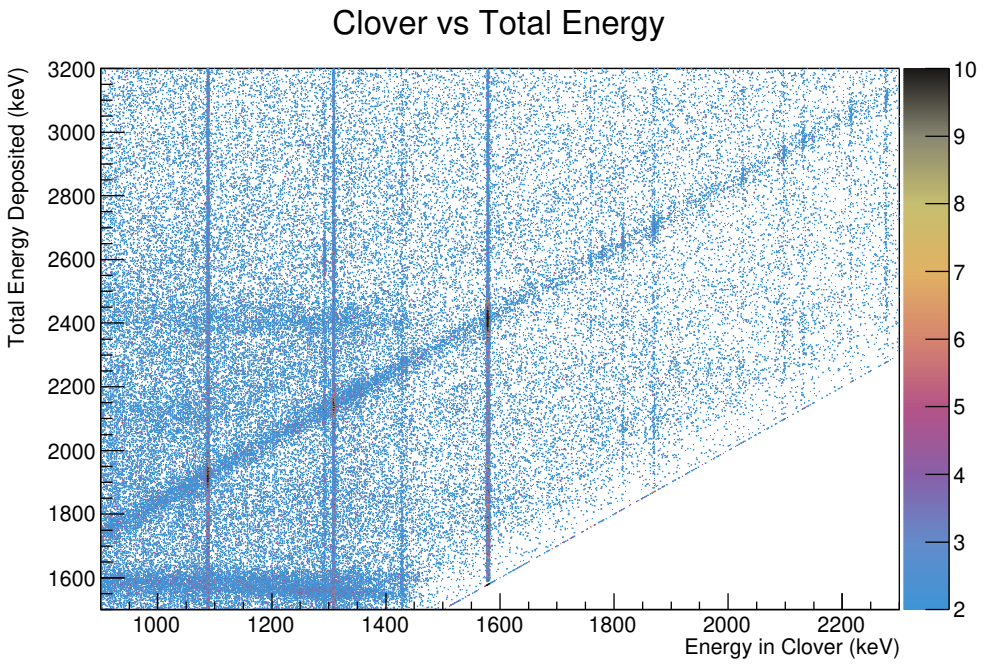


Figure 7.2: Spectrum of clover energy vs total energy deposited into the gamma-ray system for ^{94}Rb

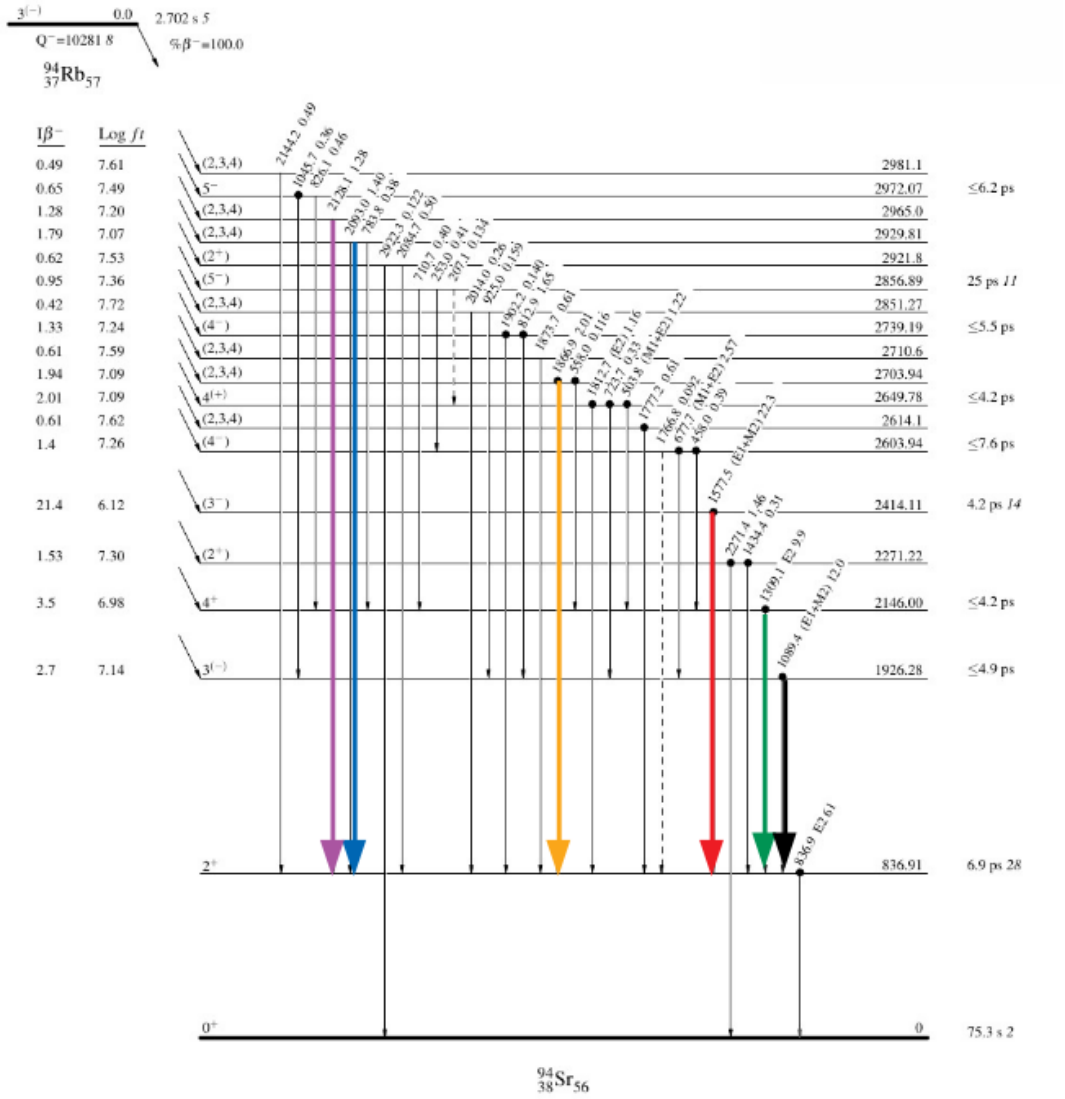
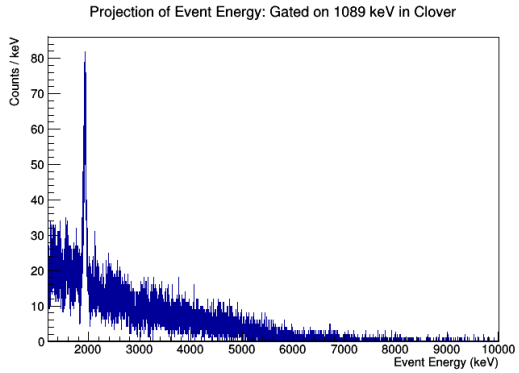
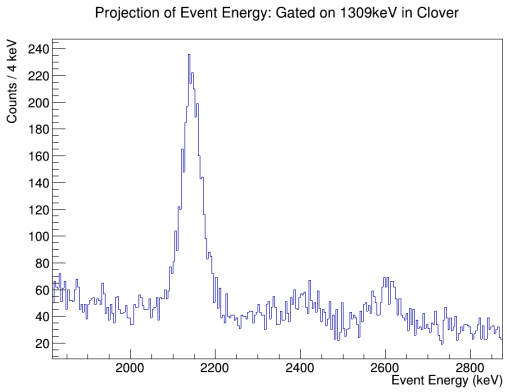


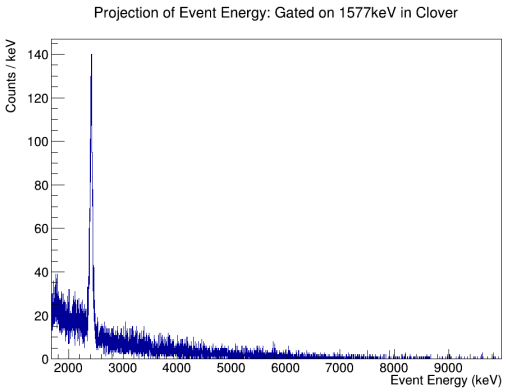
Figure 7.3: Level Diagram for ^{94}Rb. Showing only the lower 3 MeV of the nucleus. Marked are the six γ-rays shown in Figure 7.4. [34][2]



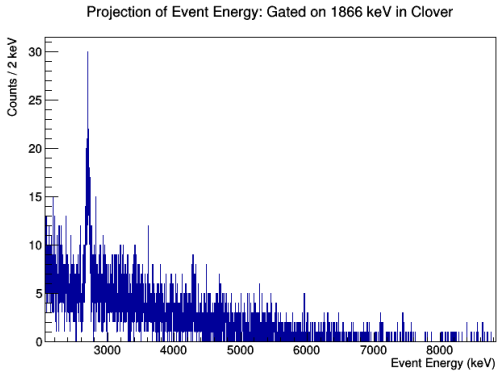
(a) Projection of the 1089 keV γ-ray in the clover onto Event energy. Shown is the 1926 keV level.



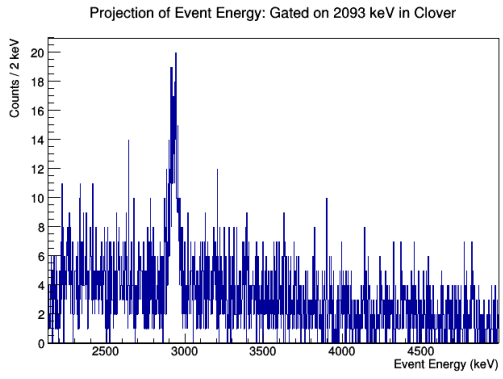
(b) Projection of the 1309 keV γ-ray in the clover onto Event energy. Shown is the 2146 keV level.



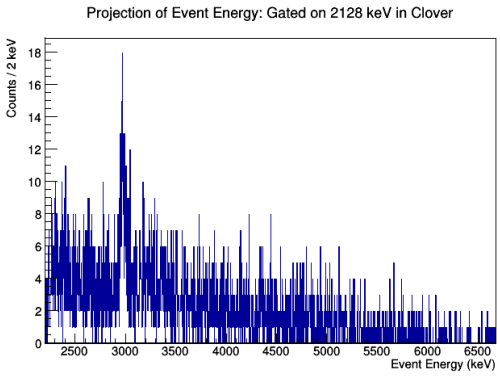
(c) Projection of the 1577 keV γ-ray in the clover onto Event energy. Shown is the 2414 keV level.



(d) Projection of the 1866.9 keV γ-ray in the clover onto Event energy. Shown is the 2703 keV level.



(e) Projection of the 2093 keV γ-ray in the clover onto Event energy. Shown is the 2929 keV level.



(f) Projection of the 2128 keV γ-ray in the clover onto Event energy. Shown is the 2965 keV level.

Figure 7.4: Results for ^{94}Sr level reconstruction

7.1.2 Neutron-γ Coincidence

Shown in Figure 7.5 is the decay scheme for ^{94}Rb β-delayed neutron emission. According to Hoff *et al.* [35], the majority of the neutron emissions leave the β-delayed neutron daughter of ^{94}Rb (^{93}Sr) in its ground state. The next most populated state is the 432.5 keV level. In Figure 7.6 of neutron time-of-flight versus QDC, we can see that the HAGRiD array greatly increases the amount of counts inside the histogram. However, the increase of counts at low QDC value is problematic because it obscures the long time-of-flight (low-energy) neutrons. One source of the additional background comes from the γ-ray detectors.

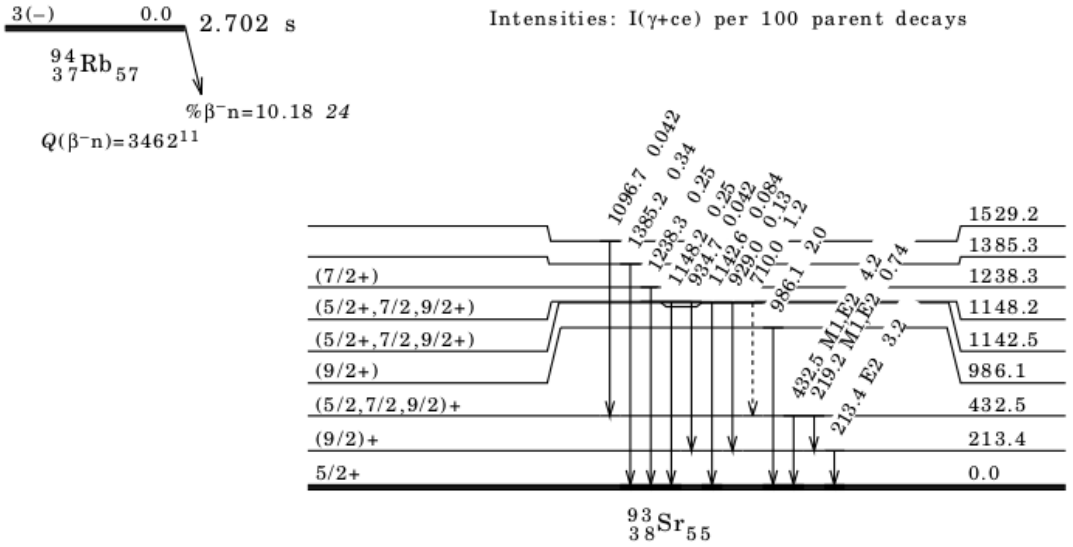


Figure 7.5: Coincident γ-ray decay scheme for ^{97}Rb βn decay [34]

The gate was adjusted to just above, and just below, the γ-ray peak and the same QDC versus ToF spectra were plotted. The resulting three spectra are projected on to the time-of-flight axis, and the average of the gates above and below is subtracted from the projection of the γ gate. Our results, shown in Figures 7.7a and 7.7b, appear to be consistent with Brady *et al.* with a peak between 100-150 ns and the intensity falling off quickly with a small shoulder at 200 ns. This was done for the four most populated states, and the results can be seen in Figure 7.8. The de-excitation of the 432.5 keV level prevents the use of HAGRiD for the 213.4 keV gate, because the 432.5 keV state has two decay paths available, one of which goes through a level at 219.2 keV. This is simply too close to the 213 keV level and causes

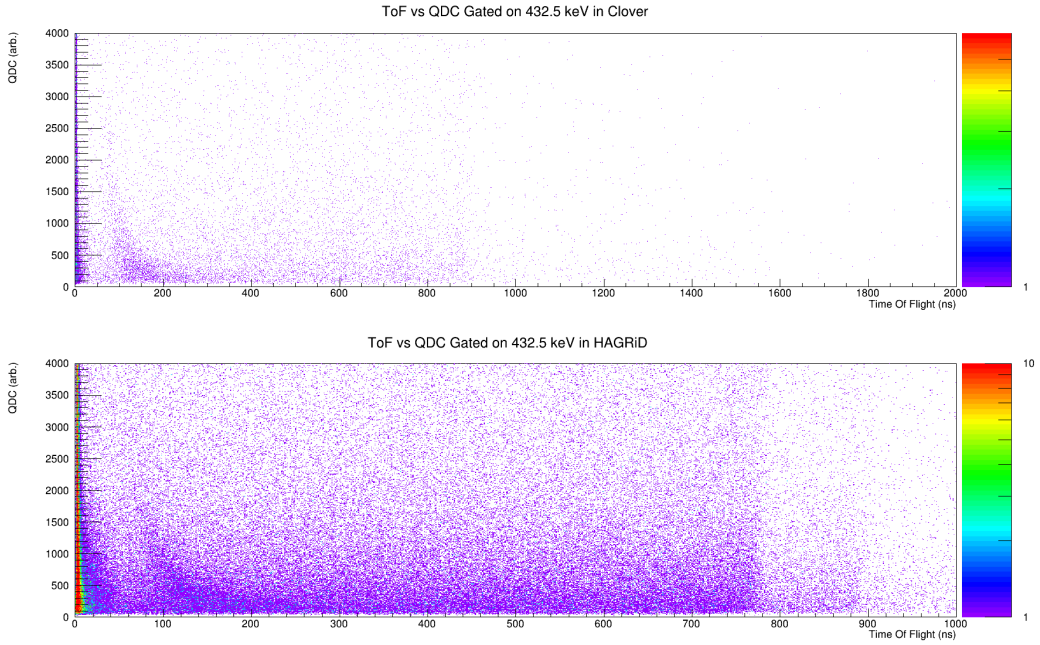
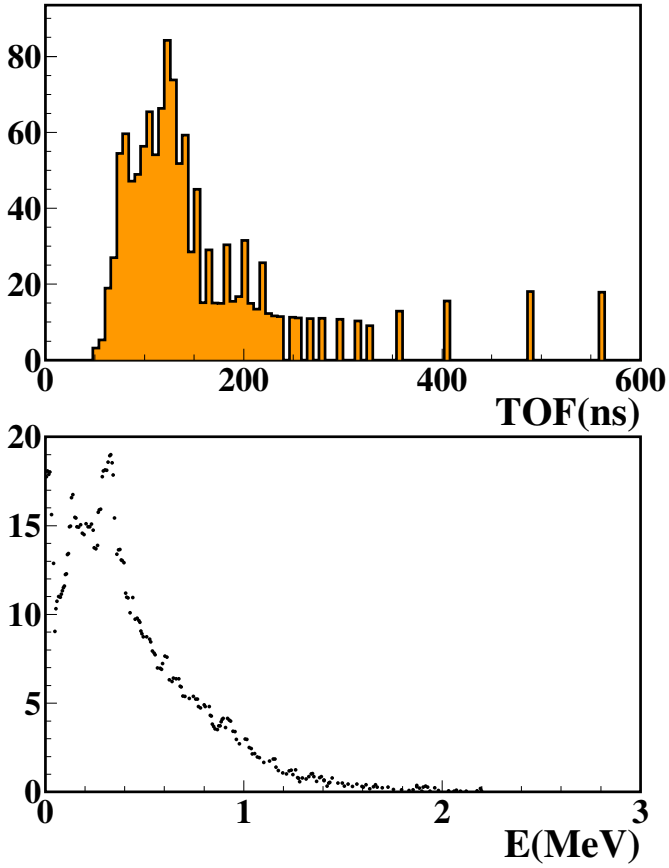
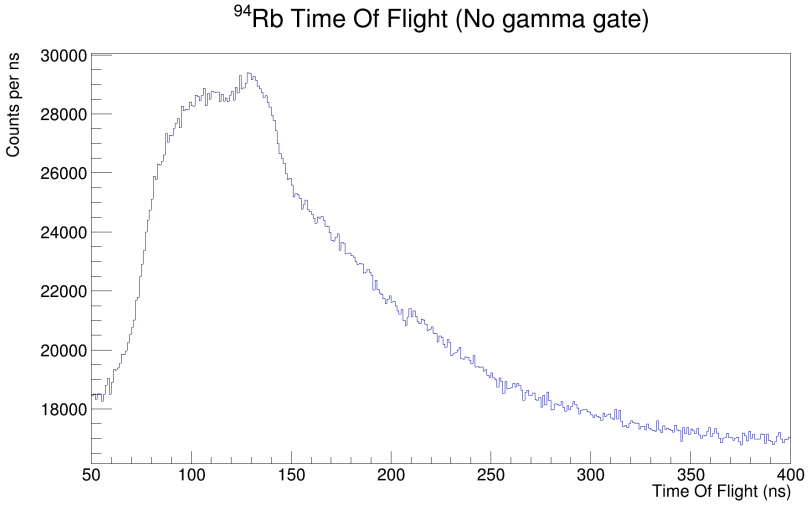


Figure 7.6: Comparison of neutron time-of-flight vs VANDLE QDC for the clover (top) and the HAGRiD (bottom) when gated on the 432.5 keV γ-ray

over-subtraction in HAGRiD as shown in Figure 7.8a. For the 1142.5 keV γ-ray there is a lack of statistics that prevents further analysis. The lack of statistics could be explained by assuming that neutrons emitted from this state have an energy below VANDLE's threshold. This appears to be a reasonable assumption based on the previous measurements by Brady *et al.* Given that VANDLE has better efficiency for higher-energy neutrons; we seem to be expanding the spectrum to include higher neutron energies, but this will need further analysis to confirm this.

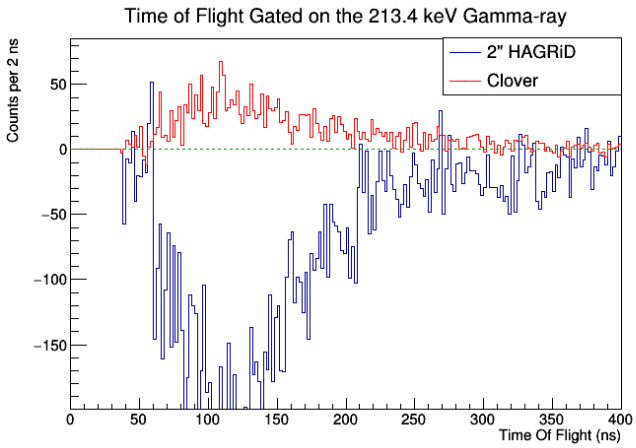


(a) ToF spectrum (upper) deduced from published energy spectrum (lower) for ^{94}Rb [26].

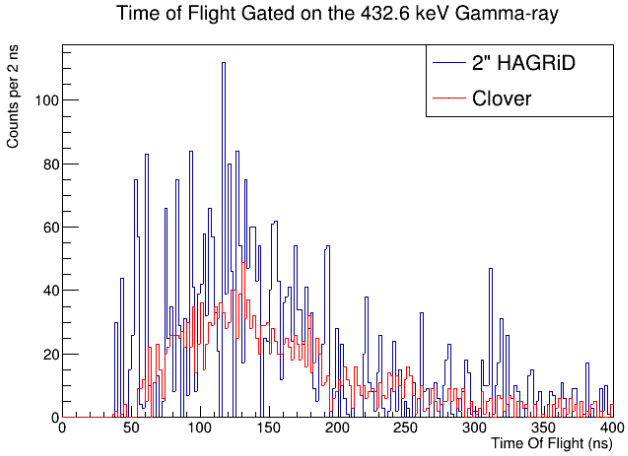


(b) Ungated ToF ^{94}Rb spectra in VANDLE

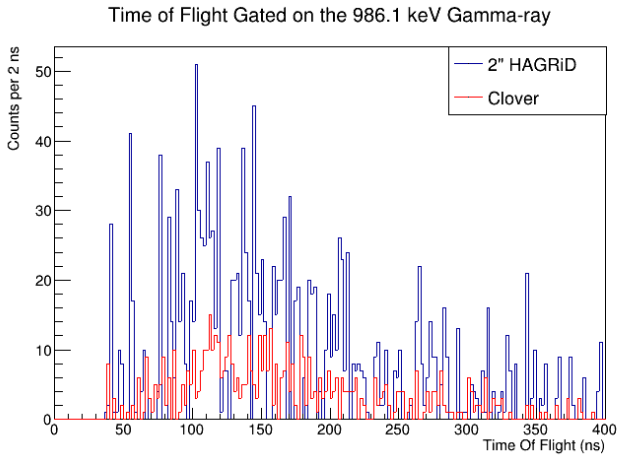
Figure 7.7: Comparison of VANDLE ToF spectrum to existing ^{94}Rb data



(a) ToF Gated with the 213.4 keV γ-ray. The 219 keV γ-ray causes over subtraction in the HAGRiD detectors



(b) ToF Gated with the 432.5 keV γ-ray



(c) ToF Gated with the 986.1 keV γ-ray

Figure 7.8: Preliminary Neutron-γ results for ^{94}Rb

7.2 ^{97}Rb

7.2.1 Neutron-γ Coincidence

For ^{97}Rb, we follow the same procedure as with ^{94}Rb. Shown in Figure 7.9 is the β-delayed neutron emission decay scheme for ^{97}Rb. According to Kratz *et al.* the β_n lines with intensities over 1% are, in decreasing intensity, 815 keV, 1506.9 keV, 1229.5 keV, 1628.2 keV, and 2150.9 keV [28].

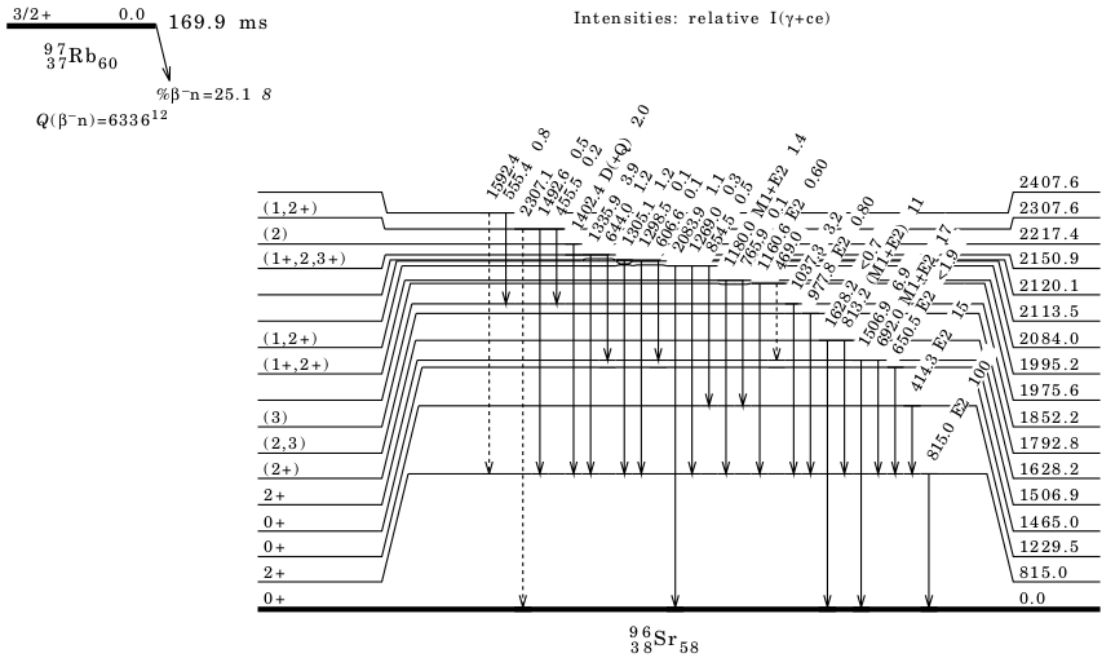


Figure 7.9: Coincident γ-ray decay scheme for ^{97}Rb βn decay [36]

As mentioned previously, in Section 3.5, the 6 second tape cycle for the high statistics run of ^{97}Rb caused significant contamination from the daughter and granddaughter. As such, we are forced to use the lower statistics run. This causes us to only able to get a subtracted time-of-flight spectrum for the most intense line, 815 keV that was reported to be 15% of the β_n decays by Kratz *et al.* [28]. Similarly to ^{94}Rb, Brady *et al.* also analyzed this nucleus. Our lack of statistics means that we can only compare the ToF spectrum for a single γ-ray transition and the shapes seem to be consistent. The spectra peak around 100 ns, and fall off with a second smaller peak between 200 and 250 ns. The addition of the second ^{97}Rb run will increase the statistics to the point where we can hopefully measure the ToF spectra for

more γ transitions. Looking again at Figure 7.10, shows us how useful the HAGRiD are to these types of low statistics measurements; since if only the clover was present this data set would be unusable in its current state. Furthermore, since the daughter and granddaughter's contributions to the neutron time-of-flight spectra is negligible compared to ^{97}Rb's; shown in Figures 7.12a and 7.12b are the time-of-flight versus VANDLE's QDC spectra for the two runs to illustrate how much extra statistics will be available once the contamination is cleaned up.

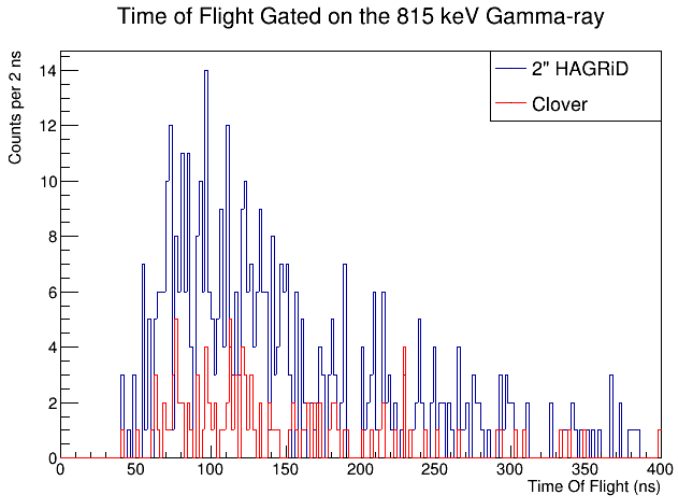
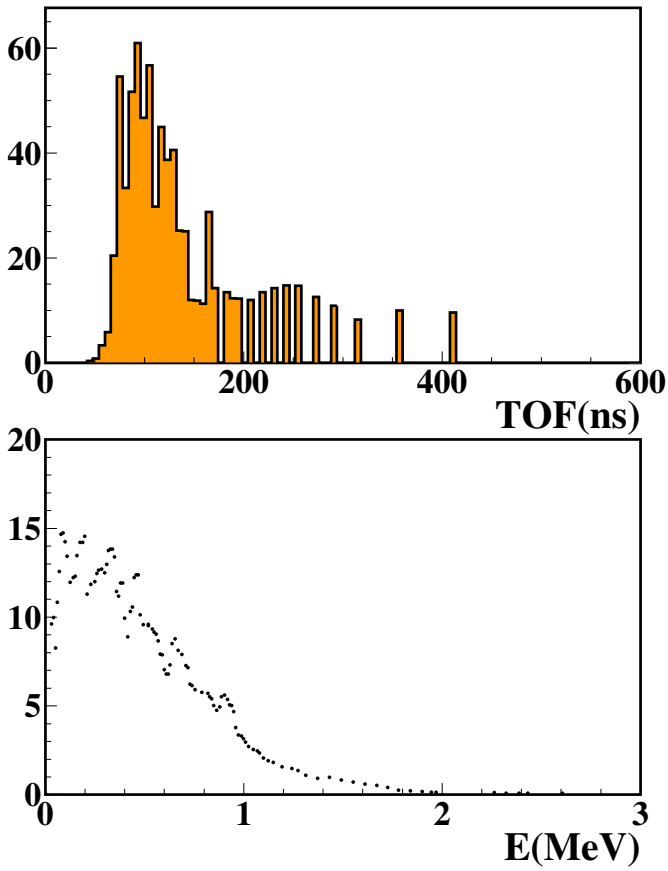
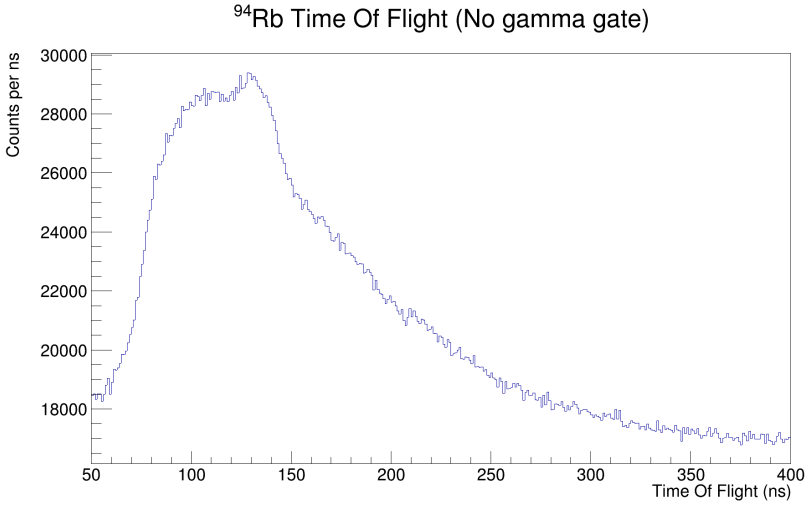


Figure 7.10: Preliminary ToF spectrum in VANDLE when gated on the 815 keV γ-ray

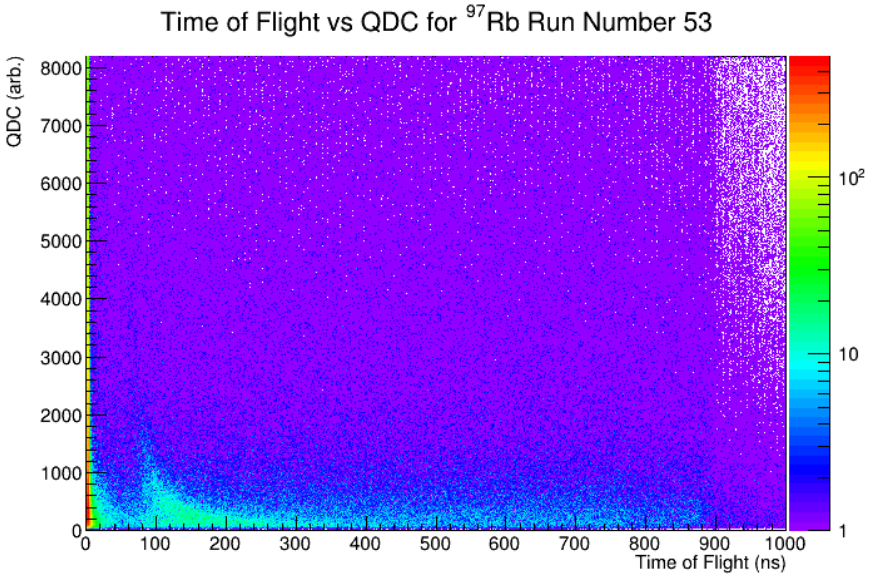


(a) ToF spectrum (upper) deduced from published energy spectrum (lower) for ^{97}Rb [26]. Y axis is counts in both figures

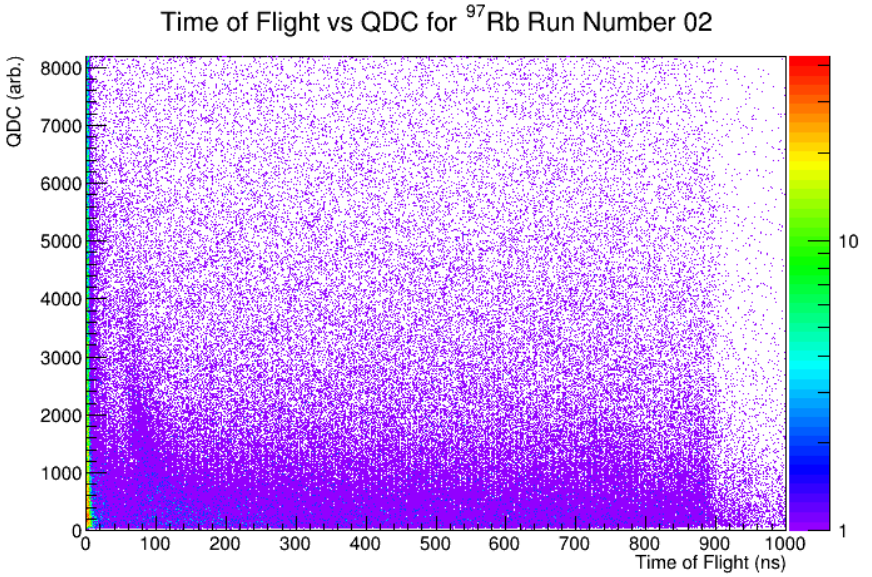


(b) Ungated ToF ^{97}Rb spectra in VANDLE

Figure 7.11: Comparison of VANDLE ToF spectrum to existing data for ^{97}Rb



(a) ToF vs QDC for Run 097rb_53



(b) ToF vs QDC for Run 097rb_02

Figure 7.12: Comparison of neutron time-of-flight vs VANDLE QDC for the high statistics (upper) and low statistics (lower) data sets

Chapter 8

Summary

This work set out to investigate the potential benefits and drawbacks of using large volume scintillators with VANDLE for β-delayed neutron measurements. Additionally the evolution of VANDLE's decay configuration as well as the upgrades for its next experiment was discussed. Changes to the VANDLE analysis methods have increased our ability to handle large data sets. This work leveraged the knowledge gained from previous VANDLE experiments to evolve the array into its current form of only medium modules for neutron detection and a mixture of high-resolution and high-efficiency γ-ray detectors.

Based on the performance of the new medium modules at ANL the arc was expanded to a full 180°. Additionally the 2nd generation SiPM based β detector with integrated MTC tape turnaround allowed for a simplified experimental setup. However due to some problems with the beam delivery, this β detector was not as efficient as it could have been. Since VANDLE has not traveled to an ISOL facility since this experiment there has not been a chance to reuse this particular detector. However, the knowledge gained has lived on in the light ion vetoes that are needed for experiments at fragmentation facilities, some of which used the same SiPM arrays which were used in the β detector. The particular configuration of VANDLE designed for this experiment was used for a subsequent run at the NSCL and served as a strong basis for an experiment at RIKEN.

At RIKEN the environment in at the experimental station necessitated a new support frame. It was also decided to upgrade the VANDLE module mounting system, because of the easy increase to the efficiency through the additional six modules. The newly available

3 inch HAGRiD detectors eliminate the need for the large NaI, while retaining most of the detector mass. Switching to the 3" detectors also allowed for the return of a second clover type HPGe detector. This should increase the efficiency for the level reconstruction. They will also augment the high-efficiency detectors in identifying γ-rays in the β_n branch that are close to states that are feed by neutron emission. An example of this is in the decay of ^{94}Rb, which has a state at 213.4keV which is feed directly as well as a state at 219.2keV, which is part of a cascade from a higher state, which is directly feed. In the low resolution gamma-ray detectors these are indistinguishable, but with the clover's resolution they are resolvable. By increasing this efficiency we are better able to compensate when this occurs.

This experiment ran successfully during the spring of 2016 and was the very last experiment to run at the Holifield Radioactive Ion Beam Facility at Oak Ridge National Laboratories before the RIB facility was decommissioned. This experiment yielded the largest VANDLE data set to date, covering several isotopes of heavy rubidium, bromine, cesium and iodine. It also provides the ability to study how shape deformation affects the β-delayed neutron emission process. The first stage of data analysis was done with the in-house software suite, PAASS; while subsequent stages were completed in ROOT. Several ROOT based programs were written to take the output of the in-house code and convert it to histograms. These ROOT codes also perform the more complex parts of the analysis such as the γ-ray reconstruction and the analysis of VANDLE events in coincidence with those in the γ-ray detectors.

Currently the high-energy γ-ray reconstruction and the hybrid analysis are separate, but this should not be difficult to fix; and this will be done in the near future. That being said, this work has shown that VANDLE is able to provide this type of data. A GEANT4 simulation of this configuration of VANDLE is currently being produced, and will provide a deeper insight into the array's response. This experiment was the first where only the medium VANDLE modules were used as well as being the first VANDLE experiment to utilize high-efficiency scintillators for γ-ray detection. The VANDLE configuration designed for this experiment was also used during later experiments at the NSCL, with only the implantation subsystem requiring major changes. It also served as the primary basis for VANDLE's RIKEN configuration.

Bibliography

[1] Joachim Krumlinde and Peter Mller. Calculation of Gamow-Teller β-strength functions in the rubidium region in the RPA approximation with Nilsson-model wave functions. *Nuclear Physics A*, 417(3):419 – 446, 1984. 1, 37

[2] NNDC. Chart of Nuclides, 2018. viii, xi, 2, 3, 59

[3] M. Kortelainen, T. Lesinski, J. Moré, W. Nazarewicz, J. Sarich, N. Schunck, M. V. Stoitsov, and S. Wild. Nuclear energy density optimization. *Phys. Rev. C*, 82:024313, Aug 2010. viii, 2

[4] Peter Möller, Bernd Pfeiffer, and Karl-Ludwig Kratz. New calculations of gross β-decay properties for astrophysical applications: Speeding-up the classical r process. *Phys. Rev. C*, 67:055802, May 2003. viii, 2

[5] Kenneth S. Krane. *Introductory Nuclear Physics*. John Wiley & Sons, Inc., 1988. 3, 5

[6] E. J. Konopinski and G. E. Uhlenbeck. On the Fermi Theory of β-Radioactivity. II. The "Forbidden" Spectra. *Phys. Rev.*, 60:308–320, August 1941. 5

[7] G. Gamow and E. Teller. Selection Rules for the β-Disintegration. *Phys. Rev.*, 49:895–899, June 1936. 5

[8] M. Madurga, S. V. Paulauskas, R. Grzywacz, D. Miller, D. W. Bardayan, J. C. Batchelder, N. T. Brewer, J. A. Cizewski, A. Fijałkowska, C. J. Gross, M. E. Howard, S. V. Ilyushkin, B. Manning, M. Matoš, A. J. Mendez, K. Miernik, S. W. Padgett, W. A. Peters, B. C. Rasco, A. Ratkiewicz, K. P. Rykaczewski, D. W. Stracener, E. H. Wang, M. Wolińska-Cichocka, and E. F. Zganjar. Evidence for Gamow-Teller Decay of ^{78}Ni Core from Beta-Delayed Neutron Emission Studies. *Phys. Rev. Lett.*, 117:092502, Aug 2016. 6, 27

[9] W. J. Huang, G. Audi, Meng Wang, F. G. Kondev, S. Naimi, and Xing Xu. The AME2016 atomic mass evaluation (i). Evaluation of input data; and adjustment procedures. *Chinese Physics C*, 41(3):030002, 2017. viii, 7

[10] Meng Wang, G. Audi, F. G. Kondev, W. J. Huang, S. Naimi, and Xing Xu. The AME2016 atomic mass evaluation (ii). Tables, graphs and references. *Chinese Physics C*, 41(3):030003, 2017. viii, 7

[11] F. Perrot, F. Maréchal, C. Jollet, Ph. Dessagne, J.-C. Angélique, G. Ban, P. Baumann, F. Benrachi, U. Bergmann, C. Borcea, A. Buţă, J. Cederkall, S. Courtin, J.-M. Daugas, L. M. Fraile, S. Grévy, A. Jokinen, F. R. Lecolley, E. Liénard, G. Le Scornet, V. Méot, Ch. Miehé, F. Negoiţă, N. A. Orr, S. Pietri, E. Poirier, M. Ramdhane, O. Roig, I. Stefan, and W. Wang. β-decay studies of neutron-rich K isotopes. *Phys. Rev. C*, 74:014313, Jul 2006. viii, 9, 10

[12] B. C. Rasco, K. P. Rykaczewski, A. Fijałkowska, M. Karny, M. Woli ńska Cichocka, R. K. Grzywacz, C. J. Gross, D. W. Stracener, E. F. Zganjar, J. C. Blackmon, N. T. Brewer, K. C. Goetz, J. W. Johnson, C. U. Jost, J. H. Hamilton, K. Miernik, M. Madurga, D. Miller, S. Padgett, S. V. Paulauskas, A. V. Ramayya, and E. H. Spejewski. Complete β-decay pattern for the high-priority decay-heat isotopes ^{137}I and ^{137}**Xe** determined using total absorption spectroscopy. *Phys. Rev. C*, 95:054328, May 2017. 9, 10

[13] M. Karny, K.P. Rykaczewski, A. Fijakowska, B.C. Rasco, M. Woliska-Cichocka, R.K. Grzywacz, K.C. Goetz, D. Miller, and E.F. Zganjar. Modular total absorption spectrometer. *Nuclear Instruments and Methods in Physics Research Section A: Accelerators, Spectrometers, Detectors and Associated Equipment*, 836:83 – 90, 2016. viii, 10, 12

[14] R. Grzywacz, K.P. Rykaczewski, C.J. Gross, M. Madurga, K. Miernik, D.T. Miller, S.V. Paulauskas, S.W. Padgett, C. Rasco, M. Wolińska-Cichocka, and E.F. Zganjar. Hybrid-3Hen New Detector for Gammas and Neutrons. *Acta Phys.Polon. B45 (2014) no.2*, page 217, 2014. viii, 11, 13

[15] A. Tarifeño-Saldivia, J. L. Tain, C. Domingo-Pardo, F. Calviño, G. Cortés, V. H. Phong, A. Riego, J. Agramunt, A. Algora, N. Brewer, R. Caballero-Folch, P. J. Coleman-Smith, T. Davinson, I. Dillmann, A. Estradé, C. J. Griffin, R. Grzywacz, L. J. Harkness-Brennan, G. G. Kiss, M. Kogimtzis, M. Labiche, I. H. Lazarus, G. Lorusso, K. Matsui,

K. Miernik, F. Montes, A. I. Morales, S. Nishimura, R. D. Page, Z. S. Podolyák, V. F.E. Pucknell, B. C. Rasco, P. Regan, B. Rubio, K. P. Rykaczewski, Y. Saito, H. Sakurai, J. Simpson, E. Sokol, R. Surman, A. Svirkhin, S. L. Thomas, A. Tolosa, and P. Woods. Conceptual design of a hybrid neutron-gamma detector for study of β-delayed neutrons at the RIB facility of RIKEN. *Journal of Instrumentation*, 12(4), 4 2017. 11

[16] A. Tolosa-Delgado and BRIKEN Collaboration. Commissioning of the BRIKEN detector for the measurement of very exotic Beta-delayed neutron emitters. *NIMA*, 2018 submitted. viii, 12, 13

[17] S. Z. Taylor. *Beta-Delayed Neutron Spectroscopy of 135-136Sb Using the Versatile Array of Neutron Detectors at Low Energy (VANDLE)*. PhD thesis, University of Tennessee, December 2018. viii, 18

[18] K. Smith, T. Baugher, S. Burcher, A.B. Carter, J.A. Cizewski, K.A. Chipps, M. Febbraro, R. Grzywacz, K.L. Jones, S. Munoz, S.D. Pain, S.V. Paulauskas, A. Ratkiewicz, K.T. Schmitt, C. Thornsberry, R. Toomey, D. Walter, and H. Willoughby. First data with the hybrid array of gamma ray detector (hagrid). *Nuclear Instruments and Methods in Physics Research Section B: Beam Interactions with Materials and Atoms*, 414:190 – 194, 2018. 20

[19] C. M. Rozsa, Peter R. Menge, and M. R. Mayhugh. BrilLanCe Scintillators Performance Summary. Technical report, Saint-Gobain Crystals, Revision: January, 2009. 20, 54

[20] S. V. Paulauskas, M. Madurga, R. Grzywacz, D. Miller, S. Padgett, and H. Tan. A digital data acquisition framework for the Versatile Array of Neutron Detectors at Low Energy (VANDLE). *NIMA*, 737(0):22 – 28, 2014. 23, 27, 53

[21] C. J. Gross, T. N. Ginter, D. Shapira, W. T. Milner, J. W. McConnell, A. N. James, J. W. Johnson, J. Mas, P. F. Mantica, R. L. Auble, J. J. Das, J. L. Blankenship, J. H. Hamilton, R. L. Robinson, Y. A. Akovali, C. Baktash, J. C. Batchelder, C. R. Bingham, M. J. Brinkman, H. K. Carter, R. A. Cunningham, T. Davinson, J. D. Fox, A. Galindo-Uribarri, R. Grzywacz, J. F. Liang, B. D. MacDonald, J. MacKenzie,

S. D. Paul, A. Piechaczek, D. C. Radford, A. V. Ramayya, W. Reviol, D. Rudolph, K. Rykaczewski, K. S. Toth, W. Weintraub, C. Williams, P. J. Woods, C.-H. Yu, and E. F. Zganjar. Performance of the Recoil Mass Spectrometer and its detector systems at the Holifield Radioactive Ion Beam Facility. *Nuclear Instruments and Methods in Physics Research A*, 450:12–29, August 2000. 24

[22] UTkLENS. Root, data analysis framework, 2016. 26

[23] Catalin Matei, D. W. Bardayan, J. C. Blackmon, J. A. Cizewski, R. K. Grzywacz, S. N. Liddick, W. A. Peters, and F. Sarazin. The versatile array of neutron detectors at low energy (vandle), 2008. 27

[24] W.A. Peters, S. Ilyushkin, M. Madurga, C. Matei, S.V. Paulauskas, R.K. Grzywacz, D.W. Bardayan, C.R. Brune, J. Allen, J.M. Allen, Z. Bergstrom, J. Blackmon, N.T. Brewer, J.A. Cizewski, P. Copp, M.E. Howard, R. Ikeyama, R.L. Kozub, B. Manning, T.N. Massey, M. Matos, E. Merino, P.D. O'Malley, F. Raiola, C.S. Reingold, F. Sarazin, I. Spassova, S. Taylor, and D. Walter. Performance of the Versatile Array of Neutron Detectors at Low Energy (VANDLE). *Nuclear Instruments and Methods in Physics Research Section A: Accelerators, Spectrometers, Detectors and Associated Equipment*, 836:122 – 133, 2016. 27, 42

[25] S. V. Paulauskas. *Beta-Delayed Neutron Spectroscopy of Fission Fragments Using the Versatile Array of Neturon Detectors at Low Energy*. PhD thesis, The University of Tennessee at Knoxville, December 2013. 27, 42

[26] M. C. Brady. *Evaluation and Application of Delayed Neutron Precursor Data*. PhD thesis, Los Alamos National Laboratory, April 1989. 36, 56, 63, 67

[27] G. Jung. *Kernspektroskopie an netronenreichen Rubidium-Spaltprodukten mit gerader Massenzahl*. PhD thesis, Justus Liebig-Universitat, Giessen, 1980. 36, 58

[28] K. L. Kratz, A. Schröder, H. Ohm, M. Zendel, H. Gabelmann, W. Ziegert, P. Peuser, G. Jung, B. Pfeiffer, K. D. Wünsch, H. Wollnik, C. Ristori, and J. Crançon. Beta-delayed neutron emission from 93–100rb to excited states in the residual Sr isotopes. *Zeitschrift für Physik A Atoms and Nuclei*, 306(3):239–257, Sep 1982. 36, 65

[29] G. Lhersonneau, B. Pfeiffer, K. L. Kratz, H. Ohm, K. Sistemich, S. Brant, and V. Paar. Structure of the N = 59 Nucleus ^{97}Sr: Coexistence of spherical and deformed states. *Z.Phys.*, A337:149, 1990. 36

[30] G. Alaga. Selection rules for beta and gamma particle transitions in strongly deformed nuclei. *Nuclear Physics*, 4:625 – 631, 1957. 37

[31] Kiefhaber. Influence of Delayed Neutron Spectra on Fast Reactor Criticality. *Nuclear Science and Engineering*, 111(2):192–204, June 1992. 37

[32] D.W Stracener, G.D Alton, R.L Auble, J.R Beene, P.E Mueller, and J.C Bilheux. Targets used in the production of radioactive ion beams at the HRIBF. *NIMA*, 521(1):126 – 135, 2004. Accelerator Target Technology for the 21st Century. Proceedings of the 21st World Conference of the International Nuclear Target Society. 39

[33] CERN. Root, data analysis framework, 2018. 45

[34] D. Abriola and A.A. Sonzogni. Nuclear Data Sheets for A = 94. *Nuclear Data Sheets*, 107(9):2423 – 2578, 2006. xi, 59, 61

[35] P. Hoff. The population of excited states in residual nuclei via delayed neutrons. *Nuclear Physics A*, 359(1):9 – 35, 1981. 61

[36] N. Nica. Nuclear Data Sheets for A = 97. *Nuclear Data Sheets*, 111(3):525 – 716, 2010. xi, 65

Vita

Thomas Tobias King was born on a warm August night in 1991 outside of Cleveland Ohio. He was born on what would have been his great-grandmother's 100th birthday. For the first few years of his life he lived just east of Cleveland in the snow belt, where 3 feet of snow while you were sleeping was a common occurrence. With all that snow, digging tunnels and building snow forts are some of his earliest and fondest childhood memories. After moving to Pittsburgh, he started playing soccer and swimming. During his time in Pittsburgh he and his father started and completed many home "improvement" projects. Then before starting high school, he was dragged south to Georgia where he continued his training in home "improvement" projects. He graduated from Whitewater High School in Fayette County Georgia. He then completed his undergraduate degree in physics with a minor in mathematics at ~~North Georgia College and State University~~ University of North Georgia. After a short stay in the private sector, he was accepted into the Graduate Physics program at the University of Tennessee in 2014 and moved over the mountains to Knoxville TN. He has since enjoyed traveling all over the world to perform experiments. As well as most days in the office.